Noble gas and carbon isotopic compositions of petit-spot lavas from southeast of Marcus Island

Yamamoto J.[a*], Kawano T.[b], Takahata N.[c] and Sano Y.[c]

[a] The Hokkaido University Museum, Nishi 8, Kita 10, Kita-ku, Sapporo 060-0810, Japan

[b] Graduate School of Science, Hokkaido University, Kita 10 Nishi 8, Kita-ku, Sapporo 060-0810, Japan

[c] Atmosphere and Ocean Research Institute, The University of Tokyo, Kashiwa, Chiba, 277-8564, Japan

*Corresponding author: Junji Yamamoto

e-mail: jyama@museum.hokudai.ac.jp

Tel.: +81-11-706-4733

Fax: +81-11-706-4029

Keywords: carbon isotopic ratio, crustal assimilation, lithosphere–asthenosphere boundary, Marcus Island, noble gases, petit-spot

Abstract

We measured noble gas isotopic compositions of quenched lavas sampled from seamounts, so-called petit-spot volcanoes, on the 160-million-year-old northwestern Pacific Plate. The samples $^{3}He/^{4}He$ and $^{40}Ar/^{36}Ar$ ratios were, respectively, 2.5–8.3 Ra and up to 1735, where Ra stands for atmospheric $^{3}He/^{4}He$, which are analogous to or lower than those of MORB. Considering narrow sampling regions, a secondary effect might be responsible for variation of the data.

During ascent and subsequent cooling of magma in the oceanic lithosphere, chemical components in the magma will be assimilated with those in the lithosphere. Correlation between $CO_2/^{3}He$ ratios and carbon isotopic ratios suggests that carbon was affected by the incorporation of seafloor carbonate. The same would be true of noble gases. The mixing of noble gases among a mantle source, an atmospheric component dissolved in seawater and a radiogenic component can explain the data distribution. No $^{3}He/^{4}He$ ratio exceeds the MORB-like value. The mantle source of the petit-spot magma was likely to have had a MORB-like $^{3}He/^{4}He$ ratio originally. The eruption of petit-spot magma shows a close relation with the bending of subducting oceanic plates. The MORB-like $^{3}He/^{4}He$ ratio supports the hypothesis that the petit-spot magma is derived from the lithosphere–asthenosphere boundary.

44 1. Introduction

45

46 The occurrence of partial melts in the lithosphere–asthenosphere boundary (LAB) is
47 an attractive hypothesis to explain a seismic low velocity zone and the high-electric
48 conductive layer in the upper mantle (Kawakatsu et al., 2009; Kumar and Kawakatsu,
49 2011; Schmerr, 2012). Moreover, this hypothesis is supported by results of
50 high-pressure experiments conducted to assess peridotite solidus (Sifré et al., 2014;
51 Wyllie, 1988) and the viscosity of silicate magma (Sakamaki et al., 2013).

52 If partial melt exists in asthenosphere, then it would migrate upward by its own
53 buoyancy and pool beneath the lithosphere (LAB). Later, it might erupt as intraplate
54 volcanoes. Batiza (1982) presents data related to the abundance, size, and crustal age of
55 volcanoes of the Pacific Ocean. The sizes of the largest seamounts are related to the age
56 of the sea floor on which they formed. Large seamounts can form on a thick lithosphere,
57 but only small seamounts form on a thin lithosphere (Hillier and Watts, 2007; Wessel,
58 1997), implying that the maximum volume and the rate at which magma can ascend
59 from the asthenosphere increases with the depth to which lithosphere-traversing
60 fractures must penetrate to reach the ponded melt (Foulger, 2010).

61 As some reports have already suggested (Hirano et al., 2006; Valentine and Hirano,
62 2010), vertical transport of the ponded melt becomes prominent when the stress state at
63 the base of the lithosphere becomes extensional, generating fractures within the
64 lithosphere. The melt will ascend through the fracture and engender volcanism along the
65 concavely flexed zone of the outer rise, outboard of the zone of plate subduction.

Additionally, horizontal migration of the ponded melt occurs because of the horizontal pressure gradient induced by the topographic head of the outer rise, sustaining a continuous melt supply to the volcanism (Yamamoto et al., 2014).

Young basalts have been discovered beside the outer rise on the northwestern Pacific Plate: so-called petit-spot volcanoes (Hirano et al., 2006). They erupted at the oceanward base of the outer rise of the descending Pacific Plate where flexure of the subducting plate causes fractures in the lithosphere (Hirano et al., 2001, 2004, 2006, 2008; Machida et al., 2015; Sato et al., 2018). Based on their geochemical signatures, these lavas presumably originated from partial melts in the asthenosphere, but the original depth of the petit-spot magma remains uncertain.

A key question is whether the petit-spot volcanoes represent LAB magma or hot spots fed by a mantle plume. Obayashi et al. (2006) studied the slow seismic velocity anomaly beneath the ocean-ward side of the Japanese subduction zone. Based on their interpretation of the seismological images, they proposed the existence of a hot thermal anomaly at the 410-km discontinuity near the Honshu subduction zone. They concluded that it is mainly an association of occurrence of fractional melt or a thermal anomaly with magnitude of approximately 200°C. The tomographically imaged low-velocity region is interpreted as a remnant of past activity of the Pacific superplume (Honda et al., 2007). However, the possible occurrence of plumes is just one interpretation of the tomographic image. Direct investigation of the magma must be conducted to settle the provenance of petit-spot magmatism.

87 Applying the $^{3}He/^{4}He$ ratio is effective for identification of the origin of petit-spot
88 magma. Mid-ocean ridge basalts (MORB) show a uniform $^{3}He/^{4}He$ ratio of 8.0 ± 1.5 Ra,
89 where Ra is atmospheric $^{3}He/^{4}He$ ratio, but $^{3}He/^{4}He$ ratios of ocean island basalts (OIB)
90 vary widely (Sano and Fischer, 2013). Although values of 20–30 Ra are common on
91 some ocean islands (i.e., Hawaii (e.g., Kaneoka et al., 2002; Valbracht et al., 1996),
92 Iceland (e.g., Moreira et al., 2001; Trieloff et al., 2000), Samoa (e.g., Farley et al., 1992;
93 Jackson et al., 2007), and Galapagos (e.g., Kurz and Geist, 1999; Kurz et al., 2009)),
94 higher $^{3}He/^{4}He$ values have been obtained for Baffin Island (e.g., up to 50 Ra; Stuart et
95 al., 2003). Moreover, enriched and HIMU-type OIBs show $^{3}He/^{4}He$ ratios lower than 8
96 Ra (Hanyu and Kaneoka, 1997; Hanyu et al., 2011). If petit-spot magma were
97 originated from LAB, then it would have a MORB-like $^{3}He/^{4}He$ ratio because the
98 original depth is comparable to that of MORB.
99 Although Hirano et al. (2006) once analyzed noble gas isotopic compositions of
100 petit-spot basaltic glasses sampled from the northwestern Pacific Plate, they did not
101 ascertain the $^{3}He/^{4}He$ ratio because of the samples low He contents and the low
102 sensitivity of the mass spectrometer for He. Recently, swarm petit-spot volcanism was
103 discovered southeast of Marcus (Minamitorishima) Island (Yokosuka YK10-05 Cruise
104 Data). The basaltic glasses have high vesicularites up to 64%, indicating higher amounts
105 of gases including He. For this study, we analyzed the $^{3}He/^{4}He$ ratios of the glasses
106 using a mass spectrometer with particular sensitivity for $^{3}He/^{4}He$ ratio. The device
107 enables us to address the origin of petit-spot magma.
108

2. Samples

During a survey (YK10-05 cruise) of the area on the northwestern Pacific Plate (Fig. 1) by the Japan Agency for Marine–Earth Science and Technology (JAMSTEC), basaltic rocks with glassy rims were recovered from petit-spot volcanoes using the manned research submersible Shinkai 6500 (Table 1). Basalts used for this study were recovered during two dives, 6K#1203 and 6K#1206, at locations about 100 km southeast of Marcus Island. Information related to sampling sites is reported in a cruise report (Yokosuka YK10-05 Cruise Data). Site 6K#1203 is located about 10 km north–northeast of the site 6K#1206. Each site covers a region with a major axis of less than approx. 1 km (Table 1). The lavas have a glassy rim with maximum thickness of approximately 3 mm. Assuming that the rate of palagonitization by seawater is 0.003–0.02 μm/year (Moore et al., 1985), 0.2–1 Ma is necessary to alter the approx. 3.0-mm thick glassy rim. Therefore the eruption age of the lavas is younger than 1 Ma.

For analyses of noble gases and carbon, only fresh glassy rims were used. Ten samples from two sites were selected based on the glassy rim freshness and thickness. All samples were collected from depths greater than 5,000 m. Figure 2 represents photomicrographs of two samples. We did not make thin sections because we strove to preserve samples to the greatest extent possible for noble gas analyses. We measured the vesicularity of the almost flat plane of the glassy rim using an area analysis option of an image histogram and image software (Photoshop®; Adobe Systems Inc.). The measured area was more than 30 mm^2 for each sample. During sample preparation for the

131 vesicularity measurement, the obtained vesicularity is somewhat higher than the true
132 value because the probability of generation of fracture within the glassy rim might be
133 biased by the occurrence of vesicles. The vesicularity is greater in the samples of
134 6K#1203 (37–64%) than in those of 6K#1206 (22–27%). The obtained high
135 vesicularities are not surprising for petit-spot lavas because similar values of 22–43%
136 were reported from the other petit-spot lavas (Okumura and Hirano, 2013). Their
137 chemical compositions have been reported elsewhere.
138
139 3. Experimental methods
140
141 Glassy rims were chipped carefully from lava samples, yielding chips of 1–7 mm.
142 Only fresh and homogeneous glasses with no visible inclusions were handpicked with
143 tweezers. After the samples were washed with acetone, they were rinsed with ethanol.
144 We did not leach the samples with HNO_3 because leaching effects would be minimal for
145 crushing experiments. After drying, the samples were weighed and loaded into the
146 degassing apparatus.
147 Gases were extracted from the glassy samples by crushing in vacuum. Before
148 crushing, mineral grains were preheated at 150°C in vacuum for 11 h. During crushing,
149 the extracted gases were exposed to a cold trap at liquid N_2 temperature to remove gases
150 that had adsorbed onto the newly created powder surfaces. Helium analyses were
151 conducted using a sector-type mass spectrometer (Helix SFT; GV Instruments Ltd.)
152 installed at the Atmosphere and Ocean Research Institute (AORI) of The University of

153 Tokyo, which is equipped with a conventional quadrupole mass spectrometer for
154 analysis of argon isotopic composition. After CO_2 was separated from other components
155 using cold traps held at liquid N_2 and ethanol-dry ice temperature, the amount of CO_2
156 and $^{13}C/^{12}C$ ratio were analyzed, respectively, using a manometer and a GC-IRMS
157 system (IsoPrime100 with vario-EA system; Isoprime Ltd.) installed at AORI. The
158 $^{13}C/^{12}C$ ratios were calibrated using a standard CO_2. Before the analysis, sulfur
159 compounds were removed using an adsorbent in EA. Sensitivities and isotopic ratios for
160 He and Ar were calibrated using an air standard. An artificial helium standard gas
161 (HESJ) with $^3He/^4He$ ratio of 20.63 ± 0.10 Ra (Matsuda et al., 2002) was also applied to
162 verify the stability of the mass spectrometer for $^3He/^4He$. Procedural crushing blanks for
163 ^4He, ^{40}Ar, and CO_2 were, respectively, less than 3.0×10^{-10}, 4×10^{-9}, and 1.6×10^{-3}
164 ccSTP. Uncertainty for all gas abundance is less than 5% in 1 σ. Analytical conditions
165 for noble gases at the AORI were described in an earlier report (Sano et al., 2008).
166
167 4. Results
168
169 Measurement results are presented in Table 2. The gas abundances vary greatly
170 among samples. Several factors affect gas abundances extracted by crushing, such as
171 the number and size of vesicles, size and quality of glass fragments, and crushing
172 efficiency. For example, sample 1206-R01 has insufficient CO_2 for analysis. This might
173 derive from both weathering and relatively low vesicularity (Table 1). However, sample

174 1206-R03, which has centimeter-sized tabular cavities in the non-glassy part (Yokosuka
175 YK10-05 Cruise Data), shows the highest gas abundance.
176 The $^{3}He/^{4}He$ ratios of the present samples are 2.5–8.3 Ra, which are analogous to or
177 much lower than the average value of Pacific MORB (8.13 ± 0.98 Ra; Graham, 2002).
178 Argon isotopic ratios ($^{40}Ar/^{36}Ar$) are higher than those for air (295.5) but much lower
179 than the MORB values, which are often up to 10,000 and which are sometimes as high
180 as 44,000 (Burnard et al., 1997; Moreira et al., 1998).
181 $\delta^{13}C$ values vary from -3.7 to +2.9‰, which is higher than that of either MORB or
182 OIB (-6.5 ± 1.7‰ (White, 2015)). The $CO_2/^{3}He$ ratio is $5.1 \times 10^{10} – 2.5 \times 10^{12}$, which is
183 much higher than that of MORB and OIB ($1 \times 10^{9}–3 \times 10^{10}$ (Jean-Baptiste et al., 2009;
184 Marty and Jambon, 1987)). Overall, no appreciable difference in gas compositions was
185 found between the samples obtained from the two dives.
186
187 5. Discussion
188
189 The principal purpose of this study was to clarify whether the petit-spot magma
190 originally has a MORB-like $^{3}He/^{4}He$ ratio. The obtained $^{3}He/^{4}He$ ratios are 2.5–8.3 Ra.
191 We evaluated them as intrinsic values of petit-spot magma.
192
193 5.1. Degassing fractionation
194

195 Magmatic degassing might influence the noble gas isotopic ratios of lavas. The
196 $^{4}He/^{40}Ar^{*}$ ratio is useful as an indicator for examining the degree of degassing of a lava
197 (Burnard et al., 2002; Cartigny et al., 2001; Marty and Zimmerman, 1999; Yamamoto
198 and Burnard, 2005). This is because $^{4}He/^{40}Ar^{*}$ ratio of the mantle is determined
199 primarily by the mantle (Th+U)/K ratio, where $^{40}Ar^{*}$ denotes ^{40}Ar corrected for air
200 contamination (defined as $^{40}Ar^{*} = {}^{36}Ar \times [(^{40}Ar/^{36}Ar)_{sample} - (^{40}Ar/^{36}Ar)_{air}]$). Therefore,
201 one can estimate the degree of magmatic degassing using $^{4}He/^{40}Ar^{*}$ ratio, over the
202 production ratio of approximately 2 (e.g., Burnard et al., 1998; Jambon et al., 1985).
203 Figure 3 depicts the degassing fractionation of $^{3}He/^{4}He$ and $^{4}He/^{40}Ar^{*}$ ratios. One
204 sample (1206-R03) shows high $^{4}He/^{40}Ar^{*}$ ratio ($^{4}He/^{40}Ar^{*} = 3.8$), which is higher than
205 the production ratio. The high $^{4}He/^{40}Ar^{*}$ ratio might be explainable by kinetic degassing
206 (Aubaud et al., 2004). Several recent reports have described that higher magmatic CO_2
207 contents enhance bubble growth and engender extensive diffusive loss of He from the
208 magma (Gonnermann and Mukhopadhyay, 2007; Weston et al., 2014). Assuming that
209 the diffusion coefficients are based on the inverse-square-root of the atomic mass,
210 diffusion-induced mass fractionation during degassing engenders preferential diffusive
211 loss of helium into vesicles, resulting in generation of vesicles for which the $^{4}He/^{40}Ar^{*}$
212 ratio is higher than that of surrounding magma. The diffusive loss of helium into
213 vesicles is accompanied by an increase in $^{3}He/^{4}He$ ratio of the vesicles (Fig. 3).
214 Assuming primary magma with MORB-like $^{3}He/^{4}He$ and $^{4}He/^{40}Ar^{*}$ ratios, the noble
215 gas isotopic composition of sample 1206-R03 cannot be reconciled with the diffusive

fractionation during kinetic degassing. Another process is necessary to interpret the data.

The kinetic degassing would be effective in interpretation of low $^{4}He/^{40}Ar^{*}$ ratio. It is noted that most samples show low $^{3}He/^{4}He$ and $^{4}He/^{40}Ar^{*}$ ratios accompanied by high $\delta^{13}C$ value and $CO_2/^{3}He$ ratios as compared with the typical mantle values. In principal, it can be explained by diffusive loss of lighter isotopes from magma. We examine the possibility based on a numerical simulation of diffusive fractionation. Figure 4 represents $^{3}He/^{4}He$ and $\delta^{13}C$ diagram of the petit-spot lava samples. We simulated the diffusive fractionation based on the model proposed by Yamamoto et al. (2009), which can calculate a fractionated elemental or isotopic ratio of a magma body bounded by two parallel planar diffusion channels. The diffusive fractionation in the magma depends on the diffusion coefficient, timescale and channel spacing. We used a diffusion coefficient for CO_2 in magma (Zhang et al., 2007). Very few studies have been done on He diffusion in silicate melts. Lux (1987) presented a diffusion coefficient for He (D_{He}) in tholeiite basalt at 1350°C as ~5×10^{-9} m^2/sec, which is roughly consistent with the extrapolated diffusivity at 1350°C proposed by Kurz and Jenkins (1981). A black broken line in Fig. 4 represents the diffusion-induced fractionation in MORB-like magma at 1350°C with channel spacing of 10 cm. It takes only one month to produce one order of magnitude lower $^{3}He/^{4}He$ ratio. In the interval, $\delta^{13}C$ value remains unchanged. The constancy in $\delta^{13}C$ results from a lower diffusion coefficient for CO_2 (D_{CO2}) in magma. The D_{CO2} in magma at 1350°C is ~1.0×10^{-11} m^2/sec (Zhang et al., 2007), resulting in D_{He}/D_{CO2} = ~500. The bubble growth driven by the

238 diffusion-induced kinetic degassing engenders a preferential change in $^{3}He/^{4}He$ ratio as
239 shown in Fig. 4. Assuming that the magma has a constant isotopic composition, it is
240 clear from the Figure 4 that the kinetic degassing cannot reproduce variation in $\delta^{13}C$
241 value. Furthermore it is impossible to explain positive values of $\delta^{13}C$ by the kinetic
242 degassing of MORB-like magma. Cartigny (1998) defined the mantle $\delta^{13}C$ value to be
243 from -8 to -2‰. Even if magma had originally had a heavier $\delta^{13}C$ value such as -2 ‰,
244 the diffusive fractionation cannot produce the positive $\delta^{13}C$ values. Though there is no
245 direct evidence to deny the influence of kinetic degassing on the present volatile
246 compositions, another mechanism is necessary to explain variation in the $^{3}He/^{4}He$ and
247 $\delta^{13}C$ values.
248
249 5.2. Air contamination
250
251 The petit-spot volcanoes are sea knolls. At the time of eruption, the possibility exists
252 of obtaining atmospheric components dissolved in seawater. To assess the possibility, it
253 is difficult to apply noble gas elemental ratios such as $^{3}He/^{36}Ar$ ratio because the
254 obtained noble gases extracted from vesicles are the result of the degassing fractionation,
255 as described in the previous section. Figure 5 presents He and Ar isotopic ratios of
256 petit-spot samples accompanied by MORB and OIB. Actually, MORB are shown along
257 a mixing line between a MORB source and air. If the $^{40}Ar/^{36}Ar$ ratio is higher than
258 approximately 300, then the atmospheric influence on $^{3}He/^{4}He$ ratio is negligible for
259 MORB (Fig. 5). In the case of OIB, during the ascent of OIB magma, noble gases in the

magma would be assimilated with those in the surrounding lithosphere (MORB source). Therefore, the distribution of OIB in Fig. 5 is explainable by three-component mixing among the OIB source, the MORB source, and air.

Atmospheric contaminants of several types might exist in oceanic basalt glasses that have identical air-like isotopic ratios, but which have different noble gas abundance ratios such as those found for air dissolved in deep-sea water, the surface atmosphere, and fractionated air infiltrated into the pore space of samples (Ballentine and Barfod, 2000; Raquin et al., 2008; Roubinet and Moreira, 2018). However, the mixing lines between the MORB source and the contaminant are mutually indistinguishable in Fig. 5. Samples obtained from each dive were collected from an individual lava flow, which originally has a homogeneous noble gas isotopic composition. Consequently, the atmospheric influence on each lava flow should be represented as a single mixing line with atmospheric contaminants. They are, however, scattered in Fig. 5. Air addition cannot be the cause of the variation of the $^{3}He/^{4}He$ ratios of the samples.

5.3. Radiogenic ingrowth

For this study, we extracted gases by crushing glass fragments in vacuum. The crushing method is probably effective for extracting gases trapped in vesicles, which contain only small amounts of in-situ generated nuclides (e.g., Graham et al., 1992a,b; Kurz, 1986). Intense crushing, however, presents the possibility of extracting radiogenic

281 nuclides accumulated within crystal lattices (Yokochi et al., 2005). We examine the
282 effects of in-situ post eruptive addition of ^{4}He on $^{3}He/^{4}He$ ratios.
283 The eruption age and the U and Th contents of the present petit-spot lavas were
284 estimated respectively as 1.1 Ma, 0.6–0.7 ppm, and 2.7–3.1 ppm (Yokosuka YK10-05
285 Cruise Data). The amount of in-situ generated ^{4}He during 1 Ma is calculated as approx.
286 2×10^{-7} ccSTP/g, which is comparable to or higher than the ^{4}He contents obtained in
287 this study (Table 2). Lava samples from this volcano show uniform U and Th contents
288 (Yokosuka YK10-05 Cruise Data), resulting in uniform ^{4}He contents (atoms/gram)
289 generated after eruption. In addition, the crushing efficiency might be almost constant
290 throughout the entire crushing because an operator did all crushing using crushing
291 vessels of the same type: radiogenic ^{4}He contents (atoms/gram) extracted by the
292 crushing would be almost constant for all samples. Lava samples with lower ^{4}He
293 contents are susceptible to the post eruptive generation of ^{4}He within the matrix.
294 Assuming that the petit-spot magma originally has a uniform $^{3}He/^{4}He$ ratio and variable
295 ^{4}He contents, the effect of the post eruptive accumulation of ^{4}He results shows a
296 negative correlation between $^{3}He/^{4}He$ ratios and ^{4}He contents. No correlation is
297 apparent in Fig. 6.
298 Correlation of noble gas isotopic compositions with vesicularity is also a useful
299 indicator to evaluate the radiogenic influence. Figure 7 depicts the $^{3}He/^{4}He$ ratio versus
300 vesicularity. The vesicularity is defined as the proportion of a vesicle volume to a given
301 volume of a lava sample. Radiogenic nuclides accumulated in the vesicles are
302 insignificant when compared to those in the lava matrix. Therefore, radiogenic

303 influences are expected to be evident on the lava samples, especially with low
304 vesicularity. No such tendency is apparent in Fig. 7. Although we cannot categorically
305 deny the radiogenic influence on $^{3}He/^{4}He$ ratios, other factors are responsible for the
306 wide distribution of $^{3}He/^{4}He$ ratios.
307
308 5.4. Crustal assimilation
309
310 The $^{3}He/^{4}He$ ratios of the petit-spot samples overlap data distribution of EM-type or
311 HIMU-type OIB rather than MORB (Fig. 5). Hanyu and Kaneoka (1997) reported
312 $^{3}He/^{4}He$ ratios of HIMU as 6.8 ± 0.9 Ra. Based on the low and uniform $^{3}He/^{4}He$ ratio,
313 they concluded that it represents a general characteristic of the mantle source region for
314 HIMU lavas. The wide variation in $^{3}He/^{4}He$ of the present petit-spot lavas dismisses the
315 possibility that the obtained $^{3}He/^{4}He$ ratios are an inherent characteristic of the
316 petit-spot magma. We next consider the possibility of crustal assimilation. Kumagai et
317 al. (2003) and Moreira et al. (2003) reported noble gas isotopic compositions of oceanic
318 crust gabbro collected from Indian Plate. The $^{3}He/^{4}He$ ratios analyzed by total melting
319 were, respectively, 0.2–8.1 and 2.9–8.2 Ra. The $^{3}He/^{4}He$ ratios of the gabbro well
320 overlap the $^{3}He/^{4}He$ ratios obtained from this study (2.5–8.3 Ra). However, it is unlikely
321 that the wide variation in the present $^{3}He/^{4}He$ ratio is caused mainly by assimilation
322 with the lower crust. We re-emphasize that, despite the narrow sampling region for each
323 site within approx. 1 km (Table 1), wide diversity of isotopic compositions is apparent.
324 Particularly, samples 1206-R03 and 1206-R04 were recovered from an almost identical

position. The isotopic compositions of the samples mutually differ. It is necessary to consider the possible influence of a local component located near the seafloor.

Although major element compositions are commonly used to assess the assimilation with local components, we applied C-He systematics for evaluation of their direct involvement to volatiles in the samples. Figure 8 shows $CO_2/^3He$ and $\delta^{13}C$ of the petit-spot samples together with end-member data for mantle (MORB and OIB), organic sediment and various types of marine limestone including slab carbonate. Assuming the C in a sample is a mixture of mantle, sediment components, and marine carbonate, we were able to make quantitative estimates of carbon contributions from those based on a mass balance calculation using $CO_2/^3He$ and $\delta^{13}C$ values as follows.

$$\delta^{13}C_O = M \cdot \delta^{13}C_M + L \cdot \delta^{13}C_L + S \cdot \delta^{13}C_S$$

$$1/(^{12}C/^3He)_O = M/(^{12}C/^3He)_M + L/(^{12}C/^3He)_L + S/(^{12}C/^3He)_S$$

$$M + L + S = 1$$

Therein, M, L, and S respectively denote the fractions of mantle, limestone, and sediment. Subscripts O, M, L, and S respectively refer to the obtained data, mantle, limestone, and sediment. Taking values of $\delta^{13}C_M = -6.5\ (\pm 2.5)$ ‰ (Sano and Marty, 1995), $\delta^{13}C_L = 0\ (\pm 3)$ ‰ (Schidlowski, 1988) and $\delta^{13}C_S = -30\ (\pm 10)$ ‰ (Sano and Marty, 1995), and $(^{12}C/^3He)_M = 1.5 \times 10^9$, $(^{12}C/^3He)_L = 1.0 \times 10^{13}$ and $(^{12}C/^3He)_S = 1.0 \times 10^{13}$ (Sano and Marty, 1995), one can calculate the contribution of carbon provided by the three components M, L, and S in the samples. Results indicate that the carbon in the samples is derived mainly from component L, which has a contribution of more than 85%.

347 However, the sampling depth (5126–5361 m: Table 1) is deeper than the carbonate
348 compensation depth (approx. 4500 m). Probably, the eruption depth is not different from
349 the sampling depth, which implies that the carbon in the samples is not derived from
350 seafloor carbonate. High $CaCO_3$ production at the shallow mid-ocean ridges produces a
351 calcareous ooze (calcium-carbonate sediments) that has been covered by the seabed.
352 Then the proportion of $CaCO_3$ can be preserved in bottom sediments as depicted in Fig.
353 9. When petit-spot magma penetrates through the oceanic plate, it must be assimilated
354 more or less with the ooze. Consequently, carbon isotopic compositions of the petit-spot
355 lava are affected by crustal assimilation, especially for a small lava body. The
356 compositions also affect other components. In the following section, we evaluate the
357 crustal assimilation effects on noble gases.
358
359 5.5. Pristine $^{3}He/^{4}He$ ratio of petit-spot magma
360
361 Assimilation with seafloor sediment is not confined to carbon materials. The relation
362 of the isotopic ratios between carbon and helium is shown in Fig. 4. The data are
363 distributed along a mixing line between a mantle component and limestone, as
364 presented in Fig. 8, indicating clearly that the crustal assimilation also affects helium.
365 We examine the original $^{3}He/^{4}He$ ratio of the samples using a diagram of $^{3}He/^{4}He$
366 versus $^{40}Ar/^{36}Ar$ ratios (Fig. 10). Noble gases in seafloor sediments can be expressed as
367 a mixture of the atmospheric component dissolved in seawater and radiogenic nuclides.
368 De Vleeschouwer et al. (2017) reported the K contents of seafloor sediments. The

averaged value of the sediments sampled at seafloor deeper than 5,000 m is 1.42 ± 0.92 wt%. Assuming that a sediment originally has an atmospheric $^{40}Ar/^{36}Ar$ ratio (295.5), ^{40}Ar of 2–8 × 10^{-5} ccSTP/g (Matsuda and Nagao, 1986) and K content of 0.5–2.3wt%, the $^{40}Ar/^{36}Ar$ ratio changes from the atmospheric value to 306–493 for 160 Ma, which is the plate age at which the present petit-spot volcano erupted. We put four seafloor sediments with gradations of radiogenic addition indicated as components A–D in Fig. 10. The mixing lines between MORB source and the components can adequately explain all the data. We cannot exclude the possibility that the data distribution can be interpreted by mixing with OIB magma as a mantle component. However, no $^{3}He/^{4}He$ ratio exceeds the MORB value. Actually, MORB magma is apparently the more likely candidate for a mantle end-member. This inference is supported by the Ne-Ar isotopic ratios corrected for air-addition that represents values similar to those of MORB (Hirano et al., 2006). Therefore we inferred that the petit-spot magma originated from a MORB-source mantle. The petit-spot magma is regarded as a melt that is extruded passively through fractures of the subducting oceanic plate. Consequently, one can reasonably infer that the petit-spot magma originated from the lithosphere–asthenosphere boundary.

Finally, we consider reasons for which the isotopic compositions of the present petit-spot lavas were affected intensely by those of seafloor sediments. The volume of lava is likely to be interrelated with the degree of crustal assimilation. The petit-spot volcanoes have been discovered as small seamounts, as implied by the name. A small lava body has a large surface area per unit lava volume, thereby increasing the

likelihood of crustal assimilation. Consequently, to elucidate the pristine chemical characteristics of the petit-spot magma, it is better to investigate a petit-spot volcano erupted on a younger oceanic plate, which has a less-radiogenic property. Further discovery of such petit-spot volcanoes is expected to provide a unique perspective to the ongoing debate related to the characteristics of the lithosphere–asthenosphere boundary.

6. Summary

We analyzed noble gas and carbon isotopic compositions of ten basaltic glasses from two submarine lava flows. They are part of the petit-spot volcanoes, which erupted within one million years at the 160-million-year-old northwestern Pacific Plate. The carbon isotopic compositions suggest that the petit-spot lavas were assimilated with calcareous ooze in seafloor sediments. The effect also bears on noble gases. The seafloor sediment on the old oceanic plate accumulates radiogenic nuclides such as ^{4}He and ^{40}Ar. Assuming radiogenic noble gas isotopic compositions of the seafloor sediment, all the data can be interpreted as a resultant of mixing between a mantle component and the seafloor sediment. The lack of ^{3}He/^{4}He ratio exceeding MORB-like value suggests that the petit-spot magma is genetically related to MORB source mantle rather than OIB source mantle. The petit-spot volcanism has been discovered beside the outer rise on the northwestern Pacific Plate, where the stress state at the base of the lithosphere becomes extensional, engendering the production of fractures. If there is ponded melt at the LAB, then the generation of fractures induces vertical transport of the LAB melt. It then

413 engenders eruption of magma with MORB-like isotopic composition. Consequently,
414 petit-spot magmatism with MORB-like isotopic compositions represents the possible
415 occurrence of a melt-rich layer beneath the oceanic lithosphere.
416
417
418 Acknowledgments
419
420 We are extremely grateful to Jens Hopp and to an anonymous reviewer, who
421 provided thoughtful comments related to the manuscript. We are deeply appreciative of
422 the cooperation of all crews, marine technicians, and shipboard scientific parties of the
423 JAMSTEC cruises (YK10-05). We also thank Dr. N. Hirano for access to a valuable
424 sample from this area. This study was supported by Grants-in-Aid for Scientific
425 Research (Nos. 26610136 and 25287139) from the Japan Society for the Promotion of
426 Science.
427
428
429 References
430
431 Amante, C., Eakins, B.W., 2008. ETOPO1 1 Arc-Minute Global Relief Model.
432 Procedures, Data Sources and Analysis, National Geophysical Data Center, NESDIS,
433 NOAA, U.S. Department of Commerce, Boulder, CO, August 2008.
434

435 Arevalo, R., McDonough, W.F., Luong, M., 2009. The K/U ratio of the silicate Earth:
436 insights into mantle composition, structure and thermal evolution. *Earth Planet. Sci.*
437 *Lett.* **278**, 361–369.
438
439 Aubaud, C., Pineau, F., Jambon, A., Javoy, M., 2004. Kinetic disequilibrium of C, He,
440 Ar and carbon isotopes during degassing of mid-ocean ridge basalts. *Earth Planet. Sci.*
441 *Lett.* **222**, 391–406.
442
443 Ballentine, C.J., Barfod, D.N., 2000. The origin of air-like noble gases in MORB and
444 OIB. *Earth Planet. Sci. Lett.* **180**, 39–48.
445
446 Batiza, R., 1982. Abundances, distribution and sizes of volcanoes in the Pacific Ocean
447 and implications for the origin of non-hotspot volcanoes. *Earth Planet. Sci. Lett.* **60**,
448 195–206.
449
450 Battani, A., 1996. Systematique des gaz rares dans les basalts de l'ocean Indien.
451 *Rapports de stage Annee 1995–1996, Universite Paris 7 denis diderot*.
452
453 Burnard, P., Graham, D., Turner, G., 1997. Vesicle-specific noble gas analyses of
454 "popping rock": implications for primordial noble gases in earth. *Science* **276**, 568–571.
455
456 Burnard, P.G., Graham, D.W., Farley, K.A., 2002. Mechanisms of magmatic gas loss

along the Southeast Indian Ridge and the Amsterdam–St. Paul Plateau. *Earth Planet*. *Sci*. *Lett*. **203,** 131–148.

Cartigny, P., Harris, J.W., Phillips, D., Girard, M., Javoy, M., 1998. Subduction-related diamonds? —The evidence for a mantle-derived origin from coupled $\delta^{13}C$—$\delta^{15}N$ determinations. *Chem*. *Geol*. **147**, 147–159.

Cartigny, P., Jendrzejewski, N., Pineau, F., Petit, E., Javoy, M., 2001. Volatile (C, N, Ar) variability in MORB and the respective roles of mantle source heterogeneity and degassing: the case of the Southwest Indian Ridge. *Earth Planet*. *Sci*. *Lett*. **194,** 241–257.

Craig, H., Lupton, J.E., 1976. Primordial neon, helium, and hydrogen in oceanic basalts. *Earth Planet*. *Sci*. *Lett*. **31**, 369–385.

De Vleeschouwer, D., Dunlea, A.G., Auer, G., Anderson, C.H., Brumsack, H., de Loach, A., Gurnis, M., Huh, Y., Ishiwa, T., Jang, K., Kominz, M.A., März, C., Schnetger, B., Murray, R.W., Pälike, H., Expedition 356 Shipboard Scientists., 2017. Quantifying K, U, and Th contents of marine sediments using shipboard natural gamma radiation spectra measured on DV JOIDES Resolution. *Geochem*. *Geophys*. *Geosys*. 10.1002/2016GC006715.

479 Foulger, G.R., 2010. Plates vs Plumes: A Geological Controversy, Wiley-Blackwell, UK,
480 pp. 340.
481
482 Gale, A., Dalton, C.A., Langmuir, C.H., Su, Y., Schilling, J.-G., 2013. The mean
483 compositions of ocean ridge basalts. *Geochem. Geophys. Geosys.*
484 10.1029/2012GC004334.
485
486 Gonnermann, H.M., Mukhopadhyay, S., 2007. Non-equilibrium degassing and a
487 primordial source for helium in ocean-island volcanism. *Nature* **449**, 1037–1040.
488
489 Graham, D.W., 2002. Noble gas isotope geochemistry of Mid-Ocean Ridge and Ocean
490 Island Basalts: characterization of mantle source reservoirs. *Rev. Mineral. Geochem.* **47**,
491 247–317.
492
493 Graham, D.W., Humphris, S.E., Jenkins, W.J., Kurz, M.D., 1992a. Helium isotope
494 geochemistry of some volcanic rocks from Saint Helena. *Earth Planet. Sci. Lett.* **110**,
495 121–131.
496
497 Graham, D.W., Jenkins, W.J., Schilling, J.-G., Thompson, G., Kurz, M.D., Humphris,
498 S.E., 1992b. Helium isotope geochemistry of mid-ocean ridge basalts from the South
499 Atlantic. *Earth Planet. Sci. Lett.* **110**, 133–147.
500

Hanyu, T., Kaneoka, I., 1997. The uniform and low $^{3}He/^{4}He$ ratios of HIMU basalts as evidence for their origin as recycled materials. *Nature* **390**, 273–276.

Hanyu, T., Kaneoka, I., Nagao, K., 1999. Noble gas study of HIMU and EM ocean island basalts in the Polynesian region. *Geochim. Cosmochim. Acta* **63**, 1181–1201.

Hanyu, T., Dunai, T.J., Davies, G.R., Kaneoka, I., Nohda, S., Uto, K., 2001. Noble gas study of the Reunion hotspot: evidence for distinct less-degassed mantle sources. *Earth Planet. Sci. Lett.* **193**, 83–98.

Hanyu, T., Johnson, K.T.M., Hirano, N., Ren, Z.-Y., 2007. Noble gas and geochronology study of the Hana Ridge, Haleakala volcano, Hawaii; implications to the temporal change of magma source and the structural evolution of the submarine ridge. *Chem. Geol.* **238**, 1–18.

Hanyu, T., Tatsumi, Y., Kimura, J., 2011. Constraints on the origin of the HIMU reservoir from He–Ne–Ar isotope systematics. *Earth Planet. Sci. Lett.* **307**, 377–386.

Hillier, J.K., Watts, A.B., 2007. Global distribution of seamounts from ship-track bathymetry data. *Geophys. Res. Lett.* **34**, L13304.

523 Hirano, N., Kawamura, K., Hattori, M., Saito, K., Ogawa, Y., 2001. A new type of
524 intra-plate volcanism; young alkali-basalts discovered from the subducting Pacific Plate,
525 northern Japan Trench. *Geophys*. *Res*. *Lett*. **28**, 2719–2722.
526
527 Hirano, N., Yamamoto, J., Kagi, H., Ishii, T., 2004. Young olivine xenocryst-bearing
528 alkali-basalt from the oceanward slope of the Japan Trench. *Contrib*. *Mineral*. *Petrol*.
529 **148**, 47–54.
530
531 Hirano, N., Takahashi, E., Yamamoto, J., Machida, S., Abe, N., Ingle, S., Kaneoka, I.,
532 Hirata, T., Kimura, J., Ishii, T., Ogawa, Y., Suyehiro, K., 2006. Volcanism in response to
533 plate flexure. *Science* **313**, 1426–1428.
534
535 Hirano, N., Koppers, A.A.P., Takahashi, A., Fujiwara, T., Nakanishi, M., 2008.
536 Seamounts, knolls and petit-spot monogenetic volcanoes on the subducting Pacific Plate.
537 *Basin Res*. 10.1111/j.1365-2117.2008.00363.x.
538
539 Hiyagon, H., Ozima, M., Marty, B., Zashu, S., Sakai, H., 1992. Noble gases in
540 submarine glasses from mid-oceanic ridges and Loihi seamount: Constraints on the
541 early history of the Earth. *Geochim*. *Cosmochim*. *Acta* **56**, 1301–1316.
542
543 Honda, M., Woodhead, J.D., 2005. A primordial solar-neon enriched component in the
544 source of EM-I-type ocean island basalts from the Pitcairn Seamounts, Polynesia. *Earth*

545 *Planet*. *Sci*. *Lett*. **236**, 597–612.

546

547 Honda, M., McDougall, I., Patterson, D.B., Doulgeris, A., Clague, D.A., 1993. Noble
548 gases in submarine pillow basalt glasses from Loihi and Kilauea, Hawaii: A solar
549 component in Earth. *Geochim*. *Cosmochim*. *Acta* **57**, 859–874.

550

551 Honda, S., Morishige, M., Orihashi, Y., 2007. Sinking hot anomaly trapped at the 410
552 km discontinuity near the Honshu subduction zone, Japan. *Earth Planet*. *Sci*. *Lett*. **261**,
553 565–577.

554

555 Jambon, A., Weber, H.W., Begemann, F., 1985. Helium and argon from an Atlantic
556 MORB glass: concentration, distribution and isotopic composition. *Earth Planet*. *Sci*.
557 *Lett*. **73**, 255–268.

558

559 Jean-Baptiste, P., Allard, P., Coutinho, R., Ferreira, T., Fourré, E., Queiroz, G., Gaspar,
560 J.L., 2009. Helium isotopes in hydrothermal volcanic fluids of the Azores archipelago.
561 *Earth Planet*. *Sci*. *Lett*. **281**, 70–80.

562

563 Kaneoka, I., Hanyu, T. Yamamoto, J., Miura, N.Y., 2002. Noble gas systematics of the
564 Hawaiian volcanoes based on the analysis of Loihi, Kilauea and Koolau submarine
565 rocks. in *Hawaiian Volcanoes: Deep Underwater Perspectives* (AGU Geophysical
566 Monograph **128**) ed. Takahashi E., Lipman P. W., Garcia M. O., Naka J. and Aramaki S.

373–389.

Kaneoka, I., Takaoka, N., 1978. Excess ^{129}Xe and high $^{3}He/^{4}He$ ratios in olivine phenocrysts of Kapuho lava and xenolithic dunites from Hawaii. *Earth Planet*. *Sci*. *Lett*. **39**, 382–386.

Kaneoka, I., Takaoka, N., 1980. Rare Gas Isotopes in Hawaiian Ultramafic Nodules and Volcanic Rocks: Constraint on Genetic Relationships. *Science* **208**, 1366–1368.

Kaneoka I., Takaoka N. and Upton B. G. J. (1986) Noble gas systematics in basalts and a dunite nodule from Réunion and Grande Comore Islands, Indian Ocean. *Chem*. *Geol*. **59**, 35–42.

Kawakatsu, H., Kumar, P., Takei, Y., Shinohara, M., Kanazawa, T., Araki, E., Suyehiro, K., 2009. Seismic evidence for sharp lithosphere–asthenosphere boundaries of oceanic plates. *Science* **324**, 499–502.

Kumagai, H., Kaneoka, I., 2003. Relationship between submarine MORB glass textures and atmospheric component of MORBs. *Chem*. *Geol*. **200**, 1–24.

Kumagai H., Dick, H.J.B., Kaneoka, I., 2003. Noble gas signatures of abyssal gabbros and peridotites at an Indian Ocean core complex. *Geochem*. *Geophys*. *Geosys*. **4**,

589 10.1029/2003GC000540.

590

591 Kumagai, H., Kaneoka, I., 2005. Noble gas signatures around the Rodriguez Triple
592 Junction in the Indian Ocean: constraints on magma genesis in a ridge system. *Geochim*.
593 *Cosmochim*. *Acta* **69**, 5567–5583.

594

595 Kumar, P., Kawakatsu, H., 2011. Imaging the seismic lithosphere–asthenosphere
596 boundary of the oceanic plate. *Geochem*. *Geophys*. *Geosys*. Q01006.

597

598 Kurz, M.D., 1986. Cosmogenic helium in a terrestrial igneous rock. *Nature* **320**,
599 435–439.

600

601 Kurz, M., Jenkins, W.J., 1981. The distribution of helium oceanic basaltic glasses. *Earth*
602 *Planet*. *Sci*. *Lett*. **53**, 41–54.

603

604 Kyser, T.K., Rison, W., 1982. Systematics of Rare Gas Isotopes in Basic Lavas and
605 Ultramafic Xenoliths. *J*. *Geophys*. *Res*. **87**, 5611–5630.

606

607 Lux, G., 1987. The behaviour of noble gases in silicate liquids: Solution, diffusion,
608 bubbles and surface effects, with applications to natural samples. *Geochim*. *Cosmochim*.
609 *Acta* **51**, 1549–1560.

610

611 Machida, S., Hirano, N., Sumino, H., Hirata, T., Yoneda, S., Kato, Y., 2015. Petit-spot
612 geology reveals melts in upper-most asthenosphere dragged by lithosphere. *Earth*
613 *Planet*. *Sci*. *Lett*. **426**, 267–279.
614
615 Macpherson, C.G., Hilton, D.R., Mertz, D.F., Dunai, T.J., 2005. Source, degassing, and
616 contamination of CO_2, H_2O, He, Ne, and Ar in basaltic glasses from Kolbeinsey Ridge,
617 North Atlantic. *Geochim*. *Cosmochim*. *Acta* **69**, 5729–5746.
618
619 Marty, B., Ozima, M., 1986. Noble gas distribution in oceanic basalt glasses. *Geochim*.
620 *Cosmochim*. *Acta* **50**, 1093–1097.
621
622 Marty, B., Jambon, A., 1987. $C/^3He$ in volatile fluxes from the solid Earth: implications
623 for carbon geodynamics. *Earth Planet*. *Sci*. *Lett*. **83**, 16–26.
624
625 Marty, B., Zimmermann, L., 1999. Volatiles (He, C, N, Ar) in mid-ocean ridge basalts:
626 Assessment of shallow-level fractionation and characterization of source composition.
627 *Geochim*. *Cosmochim*. *Acta* **63,** 3619–3633.
628
629 Matsuda, J., Nagao, K., 1986. Noble gas abundance in a deep-sea sediment core from
630 eastern equatorial Pacific. *Geochem*. *J*. **20**, 71–80.
631
632 Moore, J.G., Fornari, D.J., Clague, D.A., 1985. Basalts from the 1877 submarine

633 eruption of Mauna Loa, Hawaii; new data on the variation of palagonitization rate with
634 temperature. *U.S. Geological Survey Bulletin* **1663**, 11 p.
635
636 Moreira, M., Staudacher, T., Sarda, P., Schilling, J.G., Allègre, C.J., 1995. A primitive
637 plume neon component in MORB: The Shona Ridge anomaly, South Atlantic (51–52°S).
638 *Earth Planet. Sci. Lett.* **133**, 367–377.
639
640 Moreira, M., Valbracht, P.J., Staudacher, T., Allègre, C.J., 1996. Rare gas systematics in
641 Red Sea ridge basalts. *Geophys. Res. Lett.* **23**, 2453–2456.
642
643 Moreira, M., Kunz, J., Allègre, C.J., 1998. Rare gas systematics in popping rock:
644 isotopic and elemental compositions in the upper mantle. *Science* **279**, 1178–1181.
645
646 Moreira, M., Allègre, C.J., 2002. Rare gas systematics on Mid Atlantic Ridge (37–40°N).
647 *Earth Planet. Sci. Lett.* **198**, 401–416.
648
649 Moreira M., Blusztajn, J., Curtice, J., Hart, S., Dick, H., Kurz, M.D., 2003. He and Ne
650 isotopes in oceanic crust: implications for noble gas recycling in the mantle. *Earth*
651 *Planet. Sci. Lett.* **216**, 635–643.
652
653 Mukhopadhyay, S., 2012. Early differentiation and volatile accretion recorded in
654 deep-mantle neon and xenon. *Nature* **486**, 101–104.

Niedermann, S., Bach, W., 1998. Anomalously nucleogenic neon in North Chile Ridge basalt glasses suggesting a previously degassed mantle source. *Earth Planet. Sci. Lett.* **160**, 447–462.

Niedermann, S., Bach, W., Erzinger, J., 1997. Noble gas evidence for a lower mantle component in MORBs from the southern East Pacific Rise: decoupling of helium and neon isotope systematics. *Geochim. Cosmochim. Acta* **61**, 2697–2715.

Obayashi, M., Sugioka, H., Yoshimitsu, J., Fukao, Y., 2006. High temperature anomalies oceanward of subducting slabs at the 410-km discontinuity. *Earth Planet. Sci. Lett.* **243**, 149–158.

Okumura, S., Hirano, N., 2013. Carbon dioxide emission to Earth's surface by deep-sea volcanism. *Geology* **41**, 1167–1170.

Ozima, M., Zashu, S., 1983. Noble gases in submarine pillow volcanic glasses. *Earth Planet. Sci. Lett.* **62**, 24–40.

Ozima, M., Podosek, F.A., Igarashi, G., 1985. Terrestrial xenon isotope constraints on the early history of the Earth. *Nature* **315**, 471–474.

677 Péron, S., Moreira, M., Colin, A., Arbaret, L., Putlitz, B., Kurz, M.D., 2016. Neon
678 isotopic composition of the mantle constrained by single vesicle analyses. *Earth Planet*.
679 *Sci*. *Lett*. **449**, 145–154.
680
681 Petö, M.K., Mukhopadhyay, S., Kelly, K.A., 2013. Heterogeneities from the first 100
682 million years recorded in deep mantle noble gases from the Northern Lau Back-arc
683 Basin. *Earth Planet*. *Sci*. *Lett*. **369–370**, 13–23.
684
685 Poreda, R.J., Farley, K.A., 1992. Rare gases in Samoan xenoliths. *Earth Planet*. *Sci*. *Lett*.
686 **113**, 129–144.
687
688 Raquin, A., Moreira, M.A., 2009. Atmospheric $^{38}Ar/^{36}Ar$ in the mantle: implications for
689 the nature of the terrestrial parent bodies. *Earth Planet*. *Sci*. *Lett*. **287**, 551–558.
690
691 Raquin, A., Moreira, M.A., Guillon, F., 2008. He, Ne and Ar systematics in single
692 vesicles: mantle isotopic ratios and origin of the air component in basaltic glasses. *Earth*
693 *Planet*. *Sci*. *Lett*. **274**, 142–150.
694
695 Roubinet, C., Moreira, M.A., 2018. Atmospheric noble gases in Mid-Ocean Ridge
696 Basalts: identification of atmospheric contamination processes. *Geochim*. *Cosmochim*.
697 *Acta* **222**, 253–268.
698

699 Sakamaki, T., Suzuki, A., Ohtani, E., Terasaki, H., Urakawa, S., Katayama, Y.,
700 Funakoshi, K., Wang, Y., Hernlund, J.W., Ballmer, M.D., 2013. Ponded melt at the
701 boundary between lithosphere and asthenosphere. *Nature Geosci*. **6**, 1041–1044.
702
703 Sano, Y., Marty, B., 1995. Origin of carbon in fumarolic gas from island arcs. *Chem*.
704 *Geol*. **119**, 265–274.
705
706 Sano, Y., Tokutake, T., Takahata, N., 2008. Accurate measurement of atmospheric
707 helium isotopes. *Anal*. *Sci*. **24**, 521–525.
708
709 Sano, Y., Fischer, T.P., 2013. The analysis and interpretation of noble gases in modern
710 hydrothermal systems. in The Noble Gases as Geochemical Tracers, Advances in
711 Isotope Geochemistry (ed. P Burnard), pp. 391, Springer-Verlag Berlin Heidelberg,
712 Germany.
713
714 Sarda, P., Moreira, M., Staudacher, T., Schilling, J.-G., Allègre, C.J., 2000. Rare gas
715 systematics on the southernmost Mid-Atlantic Ridge: constraints on the lower mantle
716 and the Dupal source. *J*. *Geophys*. *Res*. **105**, 5973–5996.
717
718 Sarda, P., Staudacher, T., Allègre, C.J., 1988. Neon isotopes in submarine basalts. *Earth*
719 *Planet*. *Sci*. *Lett*. **91**, 73–88.
720

721 Sato, Y., Hirano, N., Machida, S., Yamamoto, J., Nakanishi, M., Ishii, T., Taki, A.,
722 Yasukawa, K., Kato, Y., 2018. Direct ascent to the surface of asthenospheric magma in a
723 region of convex lithospheric flexure. *International Geology Review*, in press.
724
725 Schidlowski, M., 1988. A 3,800-million-year isotopic record of life from carbon in
726 sedimentary rocks. *Nature* **333**, 313–318.
727
728 Schmerr, N., 2012. The Gutenberg discontinuity: Melt at the lithosphere–asthenosphere
729 boundary. *Science* **335**, 1480–1483.
730
731 Sifré, D., Gardés, E., Massuyeau, M., Hashim, L., Hier-Majumder, S., Gaillard, F., 2014.
732 Electrical conductivity during incipient melting in the oceanic low-velocity zone.
733 *Nature* **509**, 81–85.
734
735 Staudacher, T., Kurz, M.D., Allègre, C.J., 1986. New noble gas data on glass samples
736 from Loihi Seamount and Hualalai and on dunite samples from Loihi and Réunion
737 Island. *Chem*. *Geol*. **56**, 193–205.
738
739 Staudacher, T., Allègre, C.J., 1989. Noble gases in glass samples from Tahiti: Teahitia,
740 Rocard and Mehetia. *Earth Planet*. *Sci*. *Lett*. **93**, 210–222.
741
742 Staudacher, T., Sarda, P., Richardson, S.H., Allègre, C.J., Sagna, I., Dmitriev, L.V., 1989.

743 Noble gases in basalt glasses from a Mid-Atlantic Ridge topographic high at 14°N:
744 geodynamic consequences. *Earth Planet. Sci. Lett.* **96**, 119–133.
745
746 Staudacher, T., Sarda P., Allègre, C.J., 1990. Noble gas systematics of Réunion Island,
747 Indian Ocean. *Chem. Geol.* **89**, 1–17.
748
749 Stroncik, N.A., Niedermann, S., 2016a. He, Ne and Ar isotope signatures of mid-ocean
750 ridge basalts and their implications for upper mantle structure: a case study from the
751 Mid-Atlantic Ridge at 4–12°S. *Geochim. Cosmochim. Acta* **183**, 94–105.
752
753 Stroncik, N.A., Niedermann, S., 2016b. Atmospheric contamination of the primary Ne
754 and Ar signal in mid-ocean ridge basalts and its implications for ocean crust formation.
755 *Geochim. Cosmochim. Acta* **172**, 306–321.
756
757 Stroncik, N.A., Niedermann, S., Hasse, K.M., 2007. Neon and helium isotopes as
758 tracers of mantle reservoirs and mantle dynamics. *Earth Planet. Sci. Lett.* **258**, 334–344.
759
760 Stroncik, N.A., Niedermann, S., Haase, K.M., 2008. Plume-ridge interaction revisited:
761 Evidence for melt mixing from He, Ne and Ar isotope and abundance systematics.
762 *Earth Planet. Sci. Lett.* **268**, 424–432.
763
764 Stuart, F.M., Lass-Evans, S., Fitton, J.G., Ellam, R.M., 2003. High $^{3}He/^{4}He$ ratios in

765 picritic basalts from Baffin Island and the role of a mixed reservoir in mantle plumes.
766 *Nature* **424**, 57–59.
767
768 Trieloff, M., Kunz, J., Clague, D.A., Harrison, D., Allègre, C.J., 2000. The nature of
769 pristine noble gases in mantle plumes. *Science* **288**, 1036–1038.
770
771 Valbracht, P.J., Staudigel, H., Honda, M., McDougall, I., Davies, G.R., 1996. Isotopic
772 tracing of volcanic source regions from Hawaii: decoupling of gaseous from lithophile
773 magma components. *Earth Planet*. *Sci*. *Lett*. **144**, 185–198.
774
775 Valbracht, P.J., Staudacher, T., Malahoff, A., Allègre, C.J., 1997. Noble gas systematics
776 of deep rift zone glasses from Loihi Seamount, Hawaii. *Earth Planet*. *Sci*. *Lett*. **150**,
777 399–411.
778
779 Valentine, G., Hirano, N., 2010. Mechanisms of low-flux intraplate volcanic fields –
780 Basin and Range (North America) and Northwest Pacific Ocean. *Geology* **38**, 55–58.
781
782 Wessel P., 1997. Sizes and ages of seamounts using remote sensing: implications for
783 intraplate volcanism. *Science* **277**, 802–805.
784

785 Weston, B., Burgess, R., Ballentine, C.J., 2014. Disequilibrium degassing model
786 determination of the ^{3}He concentration and $^{3}He/^{22}Ne$ of the MORB and OIB mantle
787 sources. *Earth Planet. Sci. Lett.* **410**, 128–139.
788
789 White, W.M., 2015. Isotope Geochemistry. pp. 478, Wiley, West Sussex, UK.
790
791 Wyllie, P.J., 1988. Solidus curves mantle plumes and magma generation beneath Hawaii.
792 *Journal of Geophysical Research* **93**, 4171–4181.
793
794 Yamamoto, J., Burnard, P.G., 2005. Solubility controlled noble gas fractionation during
795 magmatic degassing: implications for noble gas compositions of primary melts of OIB
796 and MORB. *Geochim. Cosmochim. Acta* **69**, 727–734.
797
798 Yamamoto, J., Nishimura, K., Sugimoto, T., Takemura, K., Takahata, N., Sano, Y., 2009.
799 Diffusive fractionation of noble gases in mantle with magma channels: origin of low
800 He/Ar in mantle-derived rocks. *Earth and Planetary Science Letters* **280**, 167–174.
801
802 Yamamoto, J., Korenaga, J., Hirano, N., Kagi, H., 2014. Melt-rich
803 lithosphere–asthenosphere boundary inferred from petit-spot volcanoes. *Geology* **42**,
804 967–970. DOI:10.1130/G35944.1.
805

806 Yokochi, R., Marty, B., Pik, R., Burnard, P., 2005. High $^{3}He/^{4}He$ ratios in peridotite
807 xenoliths from SW Japan revisited: evidence for cosmogenic ^{3}He released by vacuum
808 crushing. *Geochem*. *Geophys*. *Geosys*. **6**, doi:10.1029/2004GC000836.
809
810 YOKOSUKA YK10-05 Cruise Data
811 (http://www.godac.jamstec.go.jp/darwin/cruise/yokosuka/yk10-05/e)
812
813 Zhang, Y., Xu, Z., Zhu, M., Wang, H., 2007. Silicate melt properties and volcanic
814 eruptions. *Rev*. *Geoph*. RG4004.
815
816

817 Figure captions

818

819 Figure 1. Bathymetric map of the study area. The red square represents the sampling
820 area. Topographic data are from Amante and Eakins (2008).

821

822 Figure 2. Photomicrographs of thin slabs of two petit-spot lava glasses. Scale bars show
823 1 mm. The respective vesicularities of samples 1203-R06 and 1203-R17B were 40.3
824 and 60.2%.

825

826 Figure 3. $^{3}He/^{4}He$ versus $^{4}He/^{40}Ar^{*}$ of the petit-spot lava samples, where $^{40}Ar^{*}$ denotes
827 ^{40}Ar corrected for air contamination (defined as $^{40}Ar^{*} = {}^{36}Ar \times [(^{40}Ar/^{36}Ar)_{sample} -$
828 $(^{40}Ar/^{36}Ar)_{air}]$). M denotes MORB. The $^{3}He/^{4}He$ ratio of MORB is 8.2 ± 0.7 (Hilton et
829 al., 1993). The $^{4}He/^{40}Ar^{*}$ ratio of MORB is 1.6–3.5, which is calculated as follows. The
830 radiogenic $^{4}He/^{40}Ar$ ratio of MORB, accumulated over 4.6 Gyr were calculated,
831 respectively, as 1.6, using the K/U and Th/U ratios for MORB as 12,340 (Gale et al.,
832 2013) and 3.16 (Gale et al., 2013). Possible extensive loss of ancient accumulated gas
833 would occur through strong and widespread magmatism and subsequent continental
834 growth. The accumulated $^{4}He/^{40}Ar^{*}$ ratio for 1 Gyr was 3.5. Broken lines represent
835 noble gas compositions of vesicles nucleated from magma with a MORB-like value.

836

837 Figure 4. $^{3}He/^{4}He$ and $\delta^{13}C$ diagram of the samples and end-members. End-members of
838 mantle (MORB), marine limestone (Limestone), and organic sediment (Sediment) are

839 also shown. The references of the end-members are the following: $\delta^{13}C_{Mantle}$ = -6.5 (±
840 2.5) ‰ (Sano and Marty, 1995), $\delta^{13}C_{Limestone}$ = 0 (± 3) ‰ (Schidlowski, 1988) and
841 $\delta^{13}C_{Sediment}$ = -30 (± 10) ‰ (Sano and Marty, 1995), and $(^3He/^4He)_{MORB}$ = 8.13 (± 0.98)
842 Ra (Graham, 2002). Helium in limestone and sediment are a mixture of atmospheric (1
843 Ra) and radiogenic component (< 1 Ra). Gray broken lines represent mixing lines
844 among the end-members. Error bars for the samples represent 1 σ uncertainties. A black
845 broken line represents the diffusion-controlled isotopic fractionation from magma with
846 MORB-like isotopic characteristics.
847
848 Figure 5. $^3He/^4He$ and $^{40}Ar/^{36}Ar$ diagram of the petit-spot lava samples, MORB, and
849 OIB. Error bars for the samples represent 1 σ uncertainties. Data sources were the
850 following: MORB (Battani, 1996; Craig and Lupton, 1976; Hiyagon et al., 1992;
851 Jambon et al., 1985; Kumagai and Kaneoka, 2003; 2005; Kyser and Rison, 1982;
852 Macpherson et al., 2005; Marty and Ozima, 1986; Moreira and Allègre, 2002; Moreira
853 et al., 1995; 1996; 1998; Niedermann and Bach, 1998; Niedermann et al., 1997; Ozima
854 and Zashu, 1983; Sarda et al., 2000; Stroncik and Niedermann, 2016a; 2016b; Stroncik
855 et al., 2007; 2008), Loihi (Hiyagon et al., 1992; Honda et al., 1993; Kaneoka et al.,
856 2002; Sarda et al., 1988; Staudacher et al., 1986; Valbracht et al., 1996; 1997), Kilauea
857 (Honda et al., 1993; Kaneoka and Takaoka, 1978; Kaneoka et al., 1986; 2002), Mauna
858 Loa (Valbracht et al., 1996), Hualalai (Valbracht et al., 1996), Koolau (Kaneoka et al.,
859 2002), Maui (Kaneoka and Takaoka, 1980; Kyser and Rison, 1982), Hana Ridge (Hanyu
860 et al., 2007), Iceland (Mukhopadhyay, 2012; Trieloff et al., 2000), Réunion (Hanyu et

al., 2001; Kaneoka et al., 1986; Staudacher et al., 1990), Samoa (Poreda and Farley, 1992), Cook–Austral Archipelago (Hanyu et al., 1999), Society Archipelago (Hanyu et al., 1999; Staudacher and Allègre, 1989), Pitcairn (Honda and Woodhead, 2005; Raquin and Moreira, 2009), Galapagos (Péron et al., 2016; Raquin and Moreira, 2009), and Lau Basin (Petö et al., 2013).

Figure 6. $^{3}He/^{4}He$ and ^{4}He diagram of the petit-spot lava samples.

Figure 7. $^{3}He/^{4}He$ and vesicularity of glassy rim of the petit-spot lava samples.

Figure 8. Correlation diagram for $\delta^{13}C$ and $CO_2/^{3}He$ ratios of the petit-spot lava samples. End-members of mantle (MORB and OIB), marine limestone, and organic sediment are also shown. The end-member values of $\delta^{13}C$ are the same as those in Fig. 4. The end-members values of $(^{12}C/^{3}He)$ are the following: $(^{12}C/^{3}He)_{Mantle} = 1.5 \times 10^{9}$, $(^{12}C/^{3}He)_{Limestone} = 1.0 \times 10^{13}$ and $(^{12}C/^{3}He)_{Sediment} = 1.0 \times 10^{13}$ (Sano and Marty, 1995). Dotted lines represent mixing lines among the end-members. Error bars for the samples represent 1 σ uncertainties.

Figure 9. Schematic cross-section of the oceanic lithosphere. Petit-spot lava penetrated the oceanic crust, the surface of which is covered by seafloor mud.

882 Figure 10. $^{3}He/^{4}He$ and $^{40}Ar/^{36}Ar$ diagram of the samples, MORB source, and air. Error
883 bars for the samples represent 1 σ uncertainties. A solid line shows the radiogenic
884 change of the seafloor mud, which originally has $^{3}He/^{4}He$ ratio of 1 Ra and $^{40}Ar/^{36}Ar$
885 ratio of 295.5. The radiogenic change is based on an original seafloor mud with K/U of
886 12,340 by mass (Gale et al., 2013) and Th/U ratio of 3.1 by mass (Staudacher et al.,
887 1989). Broken lines are mixing lines between the MORB source, with $^{3}He/^{4}He$ ratio of
888 8.2 Ra (Hilton et al., 1993) and $^{40}Ar/^{36}Ar$ ratio of 44,000 (Burnard et al., 1997; Moreira
889 et al., 1998), and seafloor mud components (A–D), which have $^{3}He/^{4}He$ and $^{40}Ar/^{36}Ar$
890 of (A) 0.1 Ra and 295.6, (B) 0.01 Ra and 299.3, (C) 0.0073 Ra and 400.0, and (D)
891 0.0072 Ra and 500.0.
892

Figure 1
Click here to download Figure: fig1.pdf

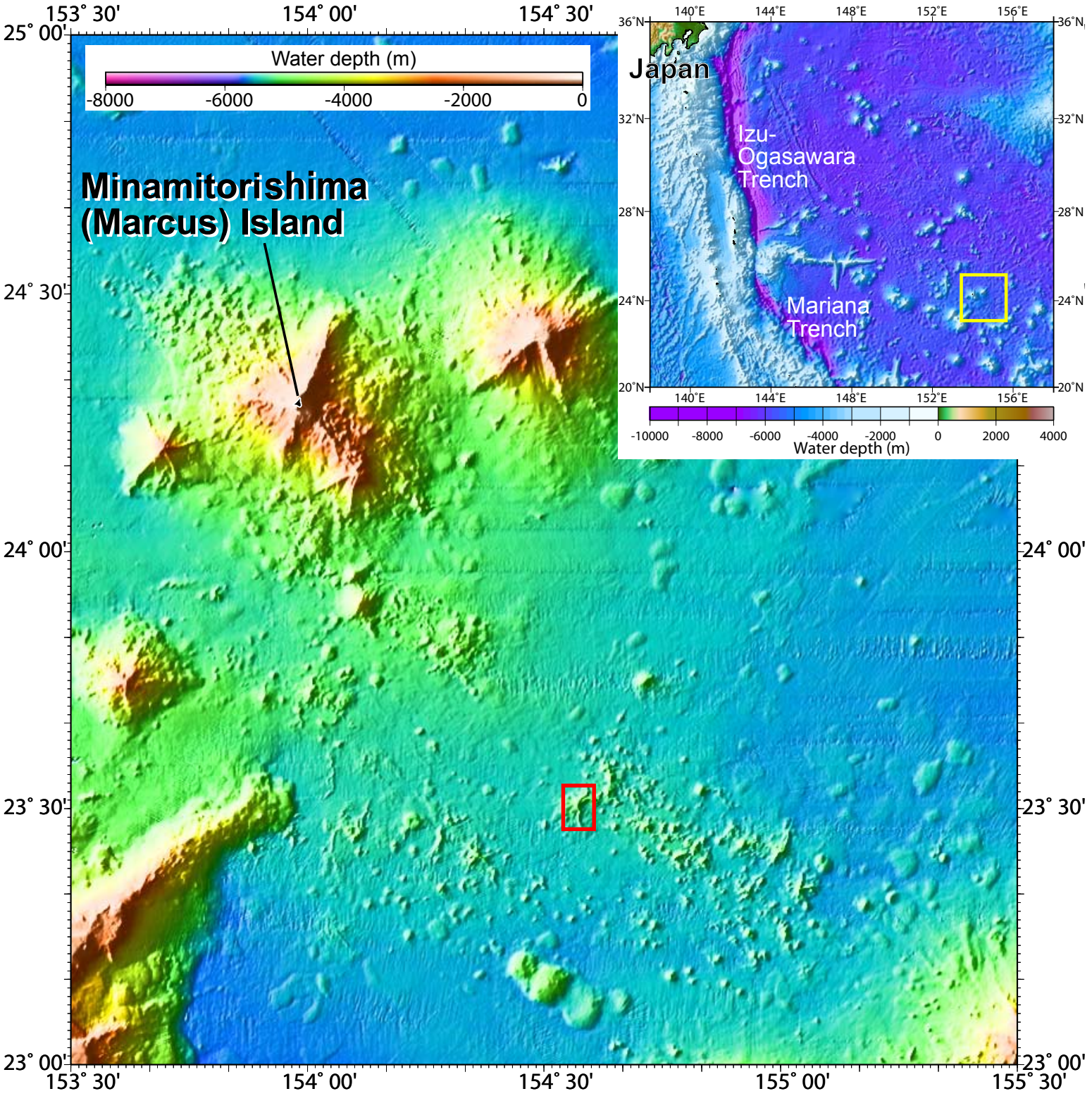

Figure 2
Click here to download high resolution image

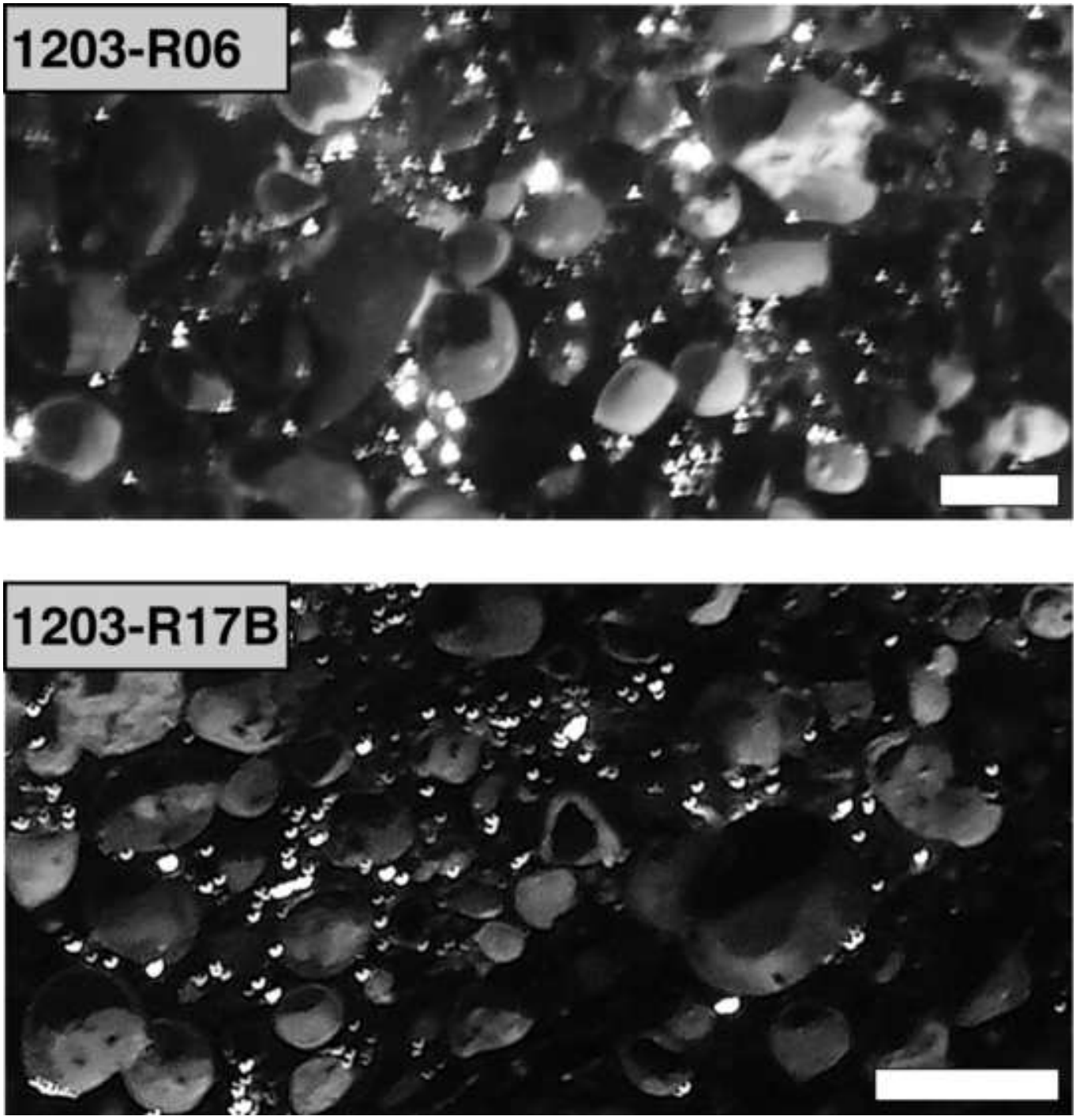

Figure 3
Click here to download high resolution image

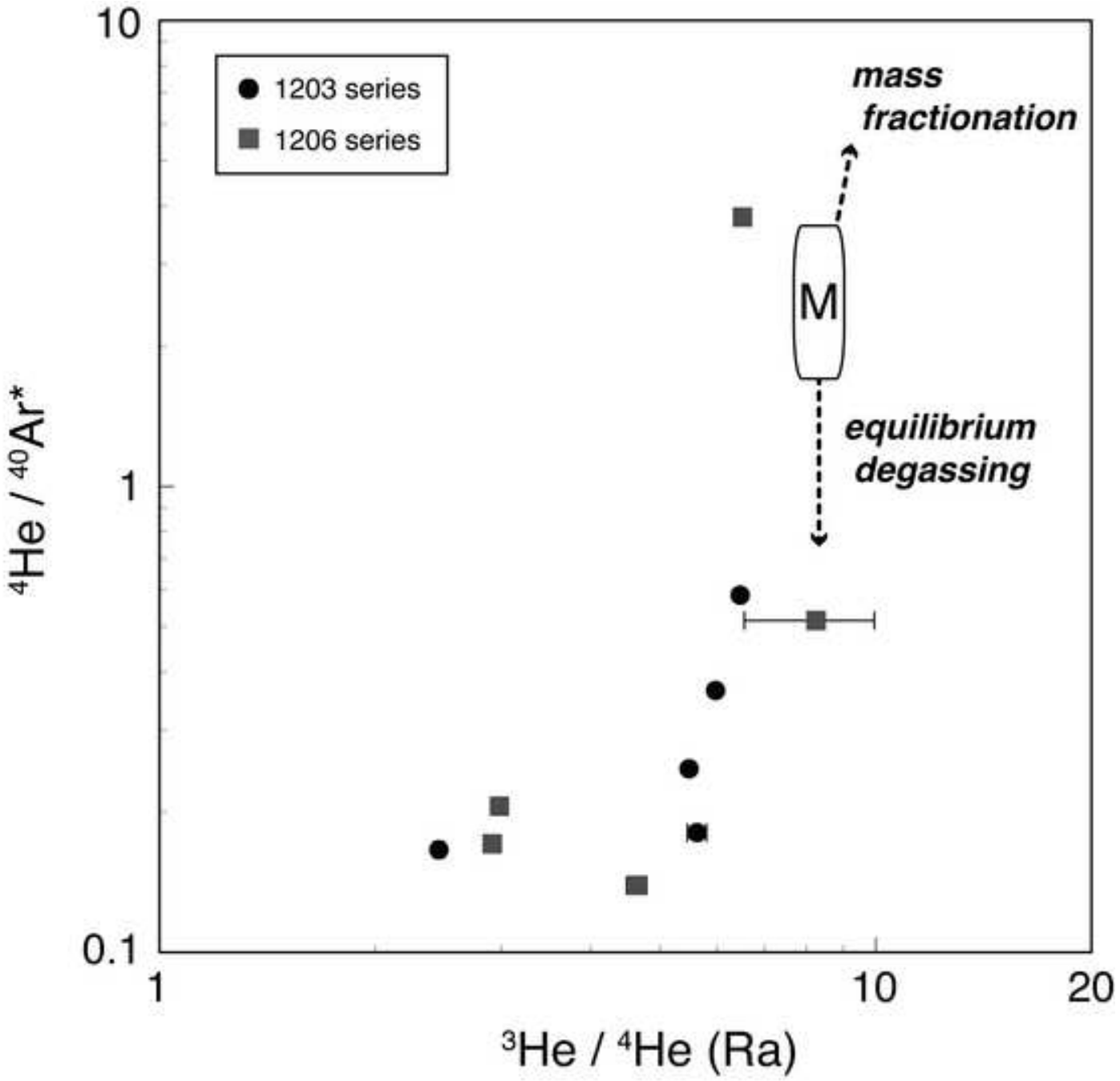

Figure 4
Click here to download high resolution image

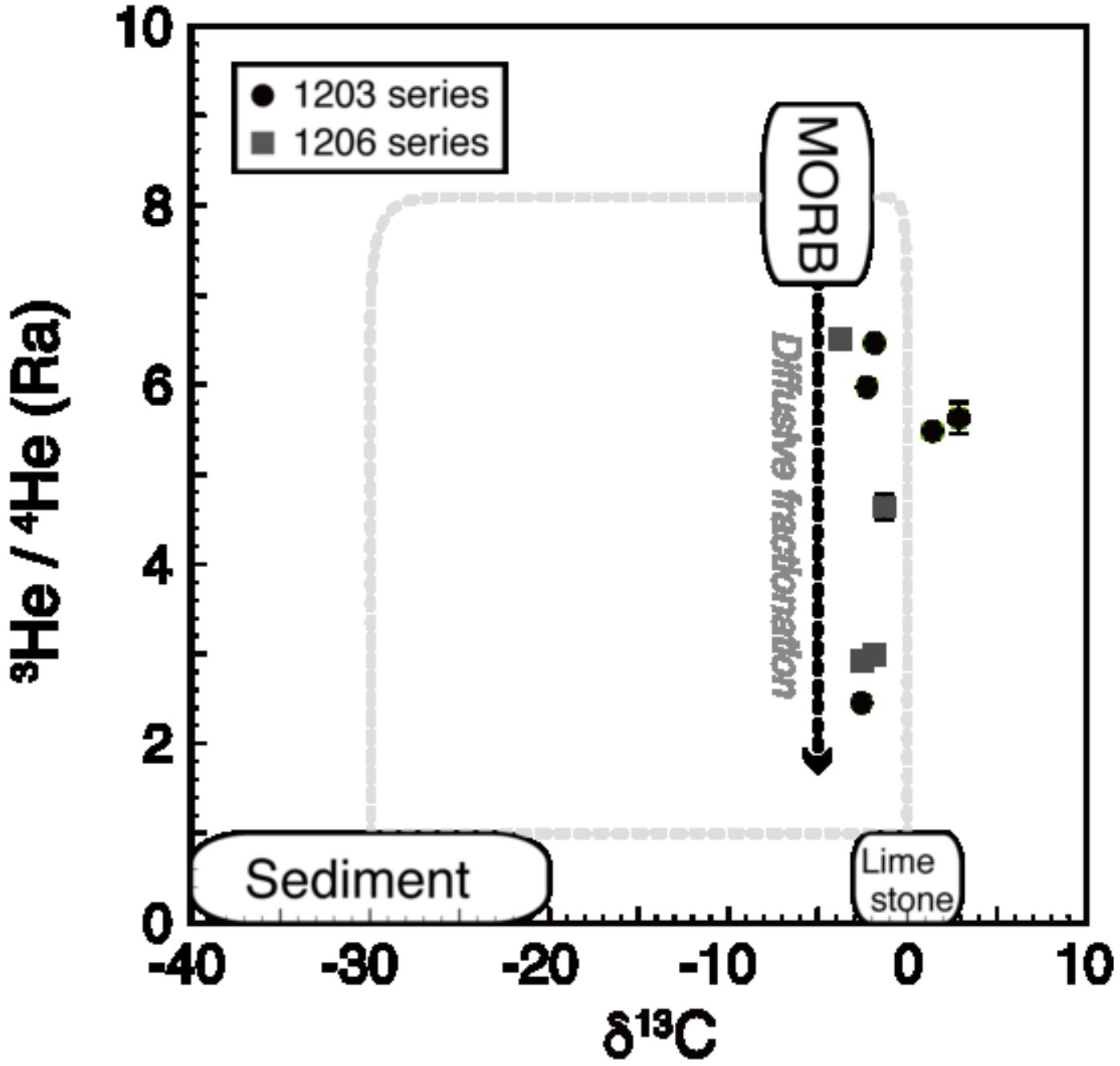

Figure 5
Click here to download high resolution image

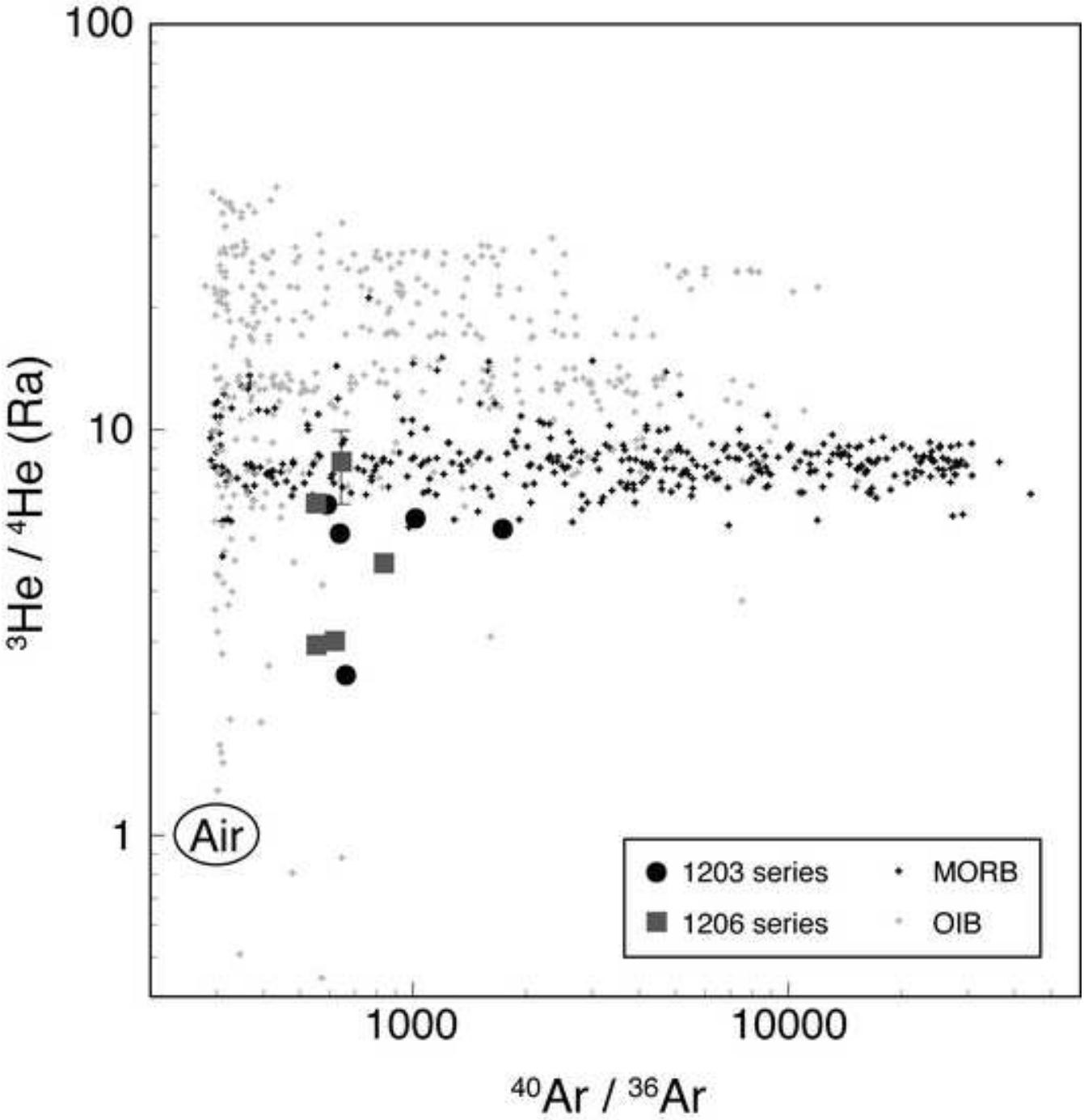

Figure 6
Click here to download high resolution image

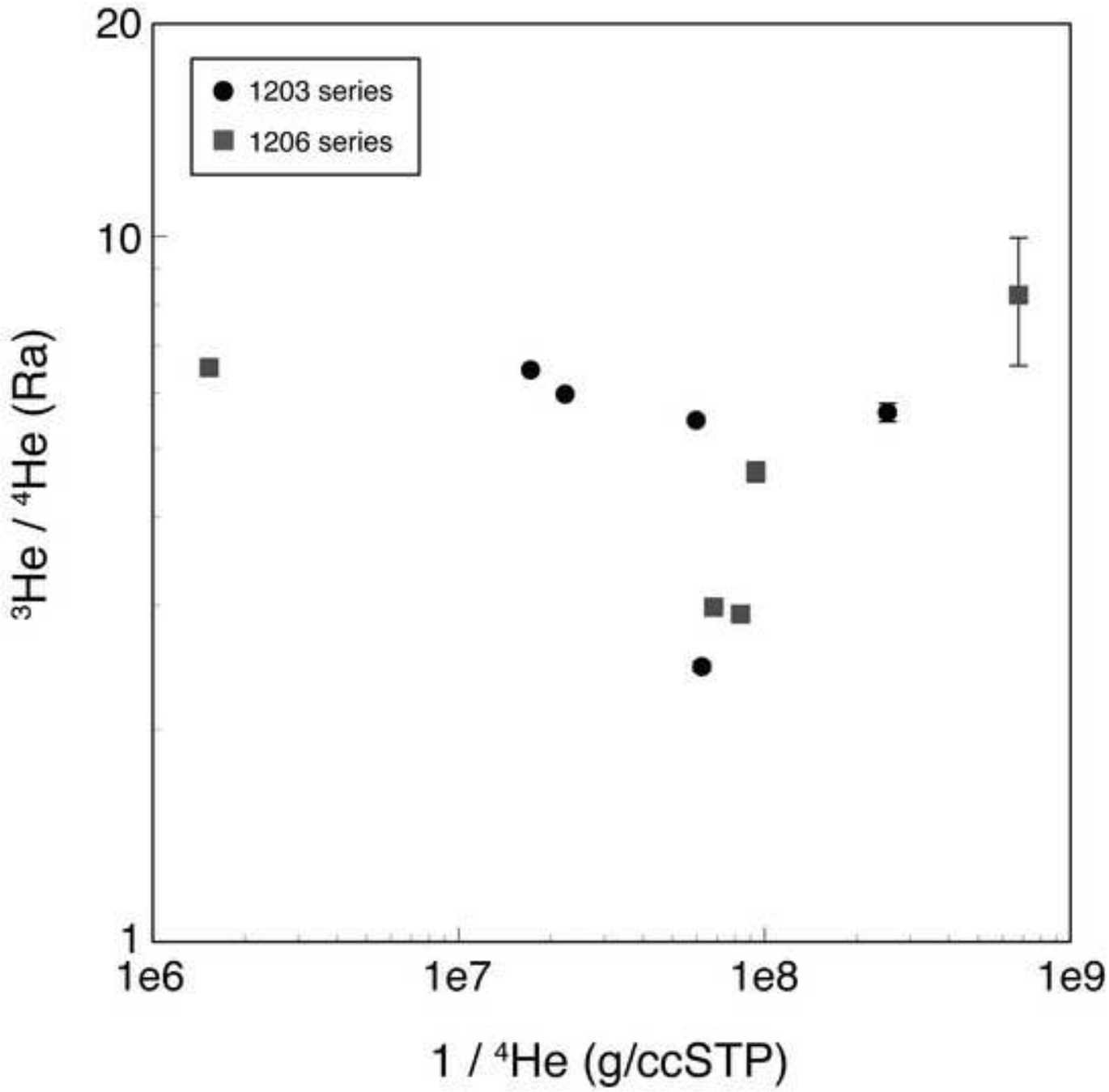

Figure 7
Click here to download high resolution image

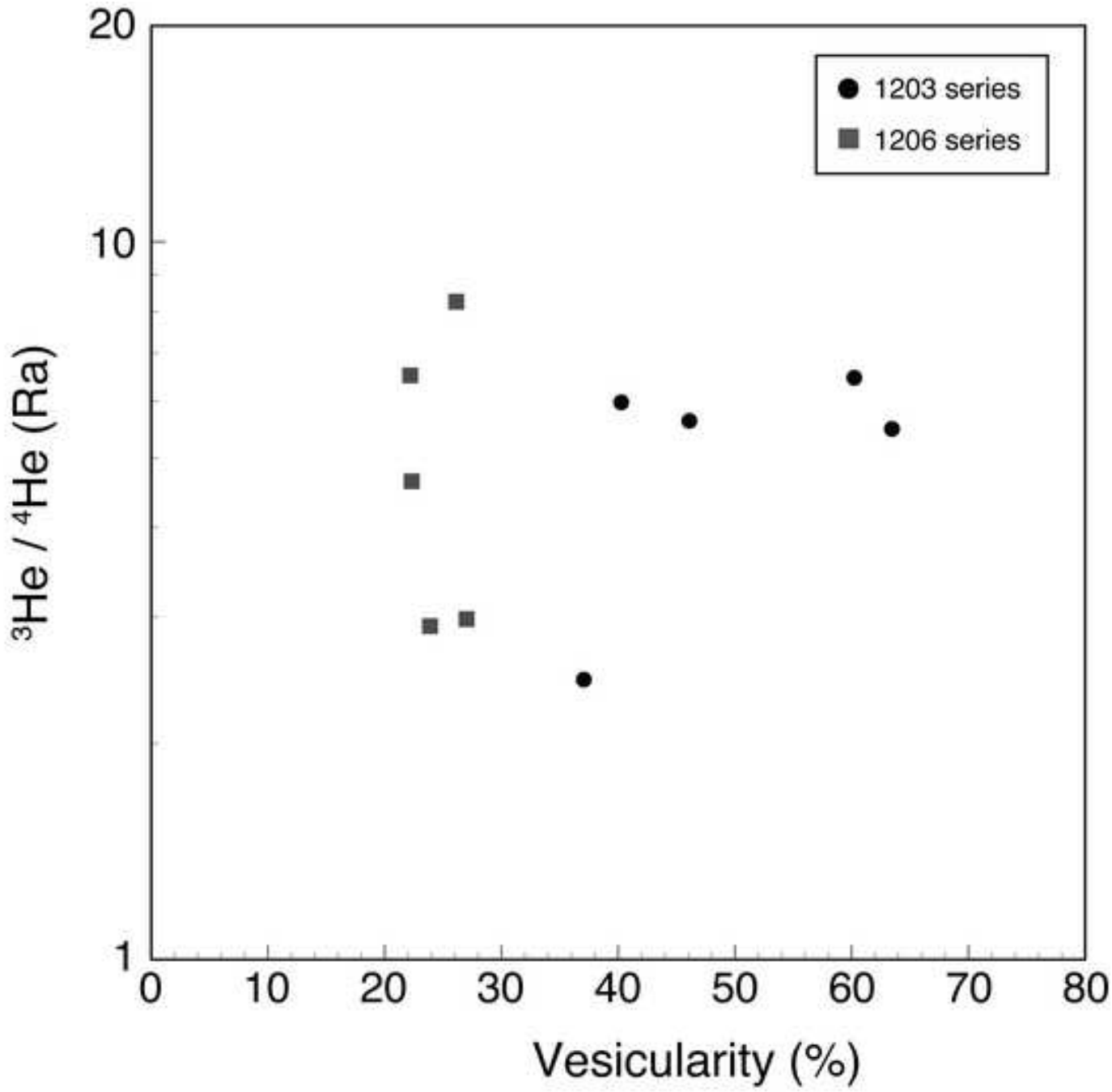

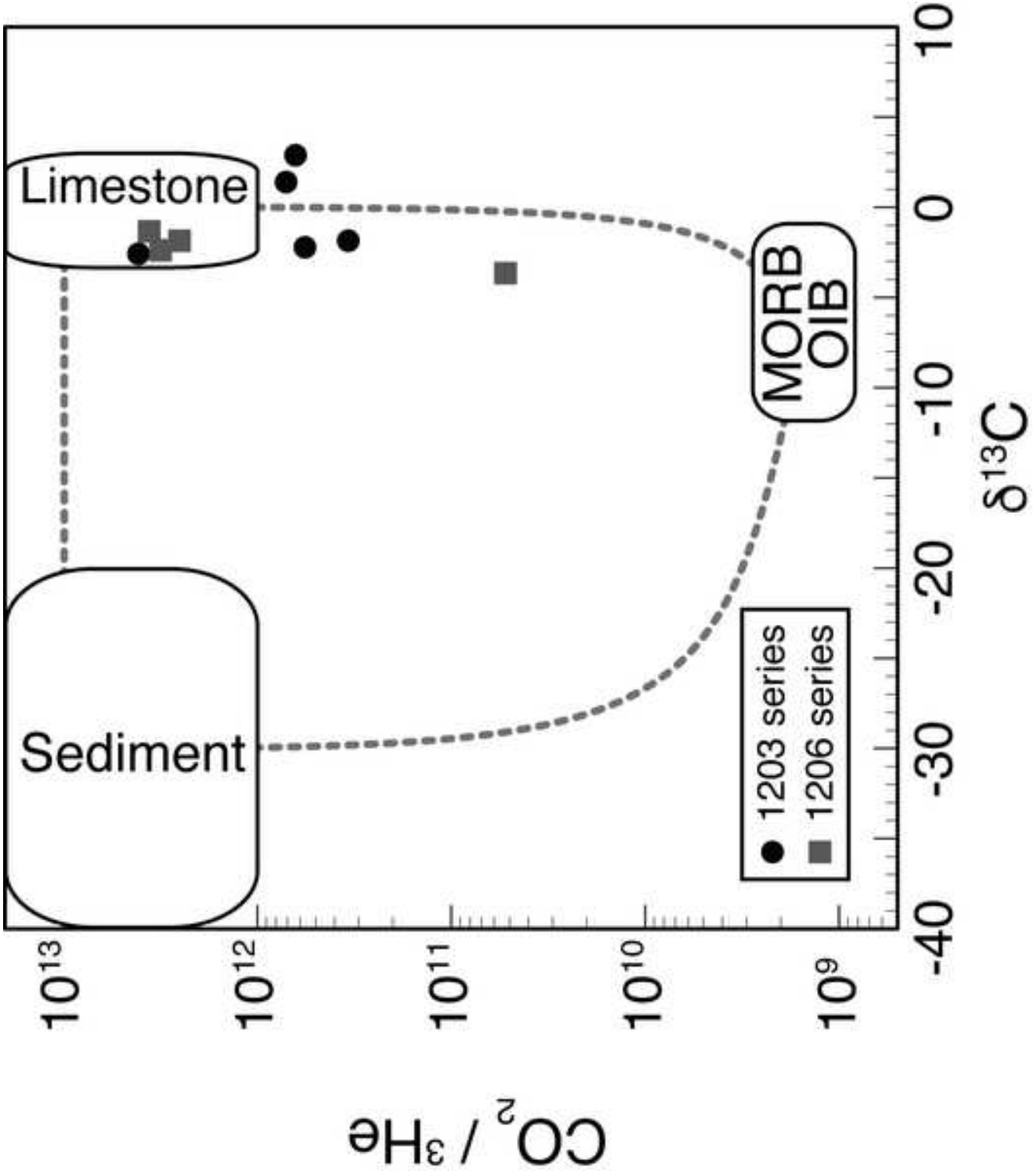

Figure 8
Click here to download high resolution image

Figure 9
Click here to download high resolution image

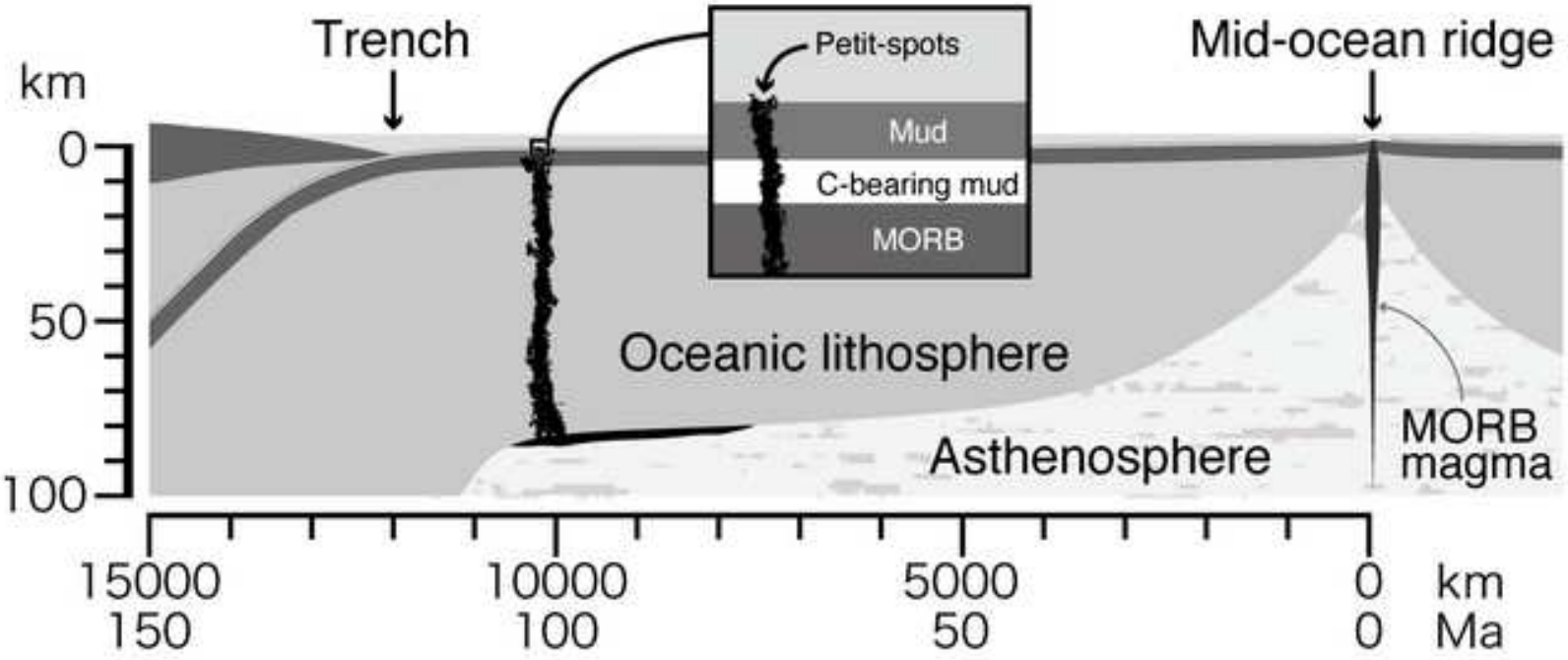

Figure 10
Click here to download high resolution image

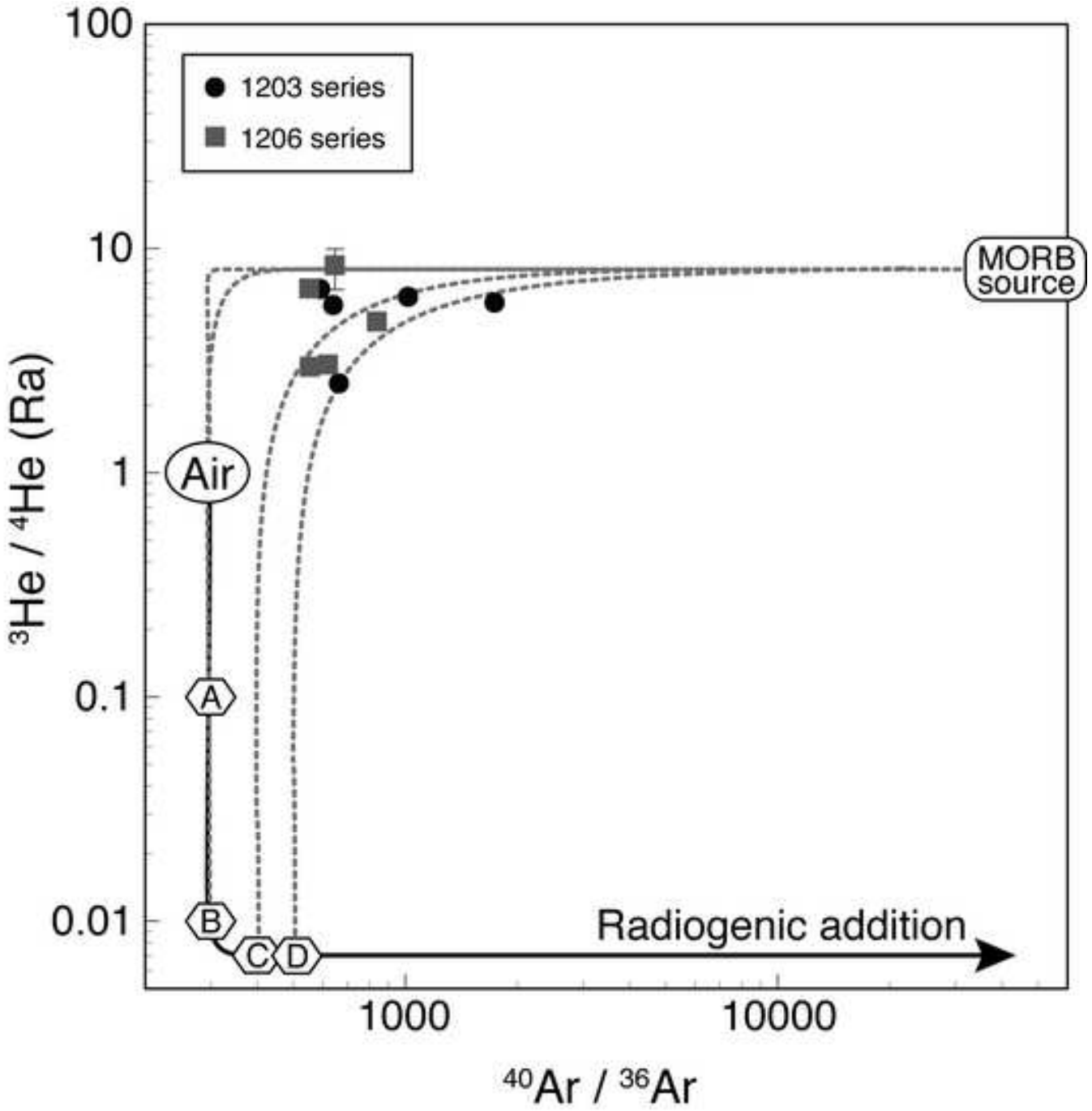

Table 1
Click here to download high resolution image

Table 1. Petit-spot samples used for noble gas analysis

Dive# 6K#1203	Latitude (°)	Longitude (°)	Depth (m)	Vesicularity (%)	Freshness
1203-R06	23.5275	154.5802	5195	40.3	very fresh
1203-R08	23.5273	154.5804	5183	37.1	fresh
1203-R10	23.5263	154.5806	5130	46.1	fresh
1203-R12	23.5263	154.5806	5130	63.5	not fresh
1203-R17B	23.5254	154.5808	5126	60.2	very fresh
Dive# 6K#1206					
1206-R01	23.4630	154.5752	5361	26.1	not fresh
1206-R03	23.4667	154.5765	5252	22.2	very fresh
1206-R04	23.4667	154.5765	5252	27.0	fresh
1206-R05	23.4671	154.5764	5247	22.3	fresh
1206-R09	23.4743	154.5738	5182	23.9	fresh

Table 2
Click here to download high resolution image

Table 2. Isotopic compositions of noble gases and carbon extracted from Petit-spot glasses

Dive# 6K#1203	weight (g)	^{4}He	^{40}Ar	CO_2	CO_2 / ^{3}He	^{3}He / ^{4}He (Ra)	^{40}Ar / ^{36}Ar	δ^{13}C (‰)
1203-R06	0.9938	4.49E-08	1.74E-07	8.95E-02	5.43E+11	5.974 ± 0.045	1016.2 ± 4.2	-2.253 ± 0.114
1203-R08	1.3772	1.60E-08	1.74E-07	9.55E-02	3.95E+12	2.455 ± 0.038	663.0 ± 2.9	-2.567 ± 0.112
1203-R10	0.9530	3.97E-09	2.65E-08	8.11E-03	6.10E+11	5.629 ± 0.171	1734.9 ± 14.5	2.871 ± 0.265
1203-R12	1.2065	1.67E-08	1.26E-07	3.85E-02	6.82E+11	5.486 ± 0.056	639.2 ± 2.8	1.388 ± 0.132
1203-R17B	1.0277	5.82E-08	2.00E-07	7.52E-02	3.25E+11	6.465 ± 0.045	590.5 ± 2.6	-1.836 ± 0.115
Dive# 6K#1206								
1206-R01	0.4809	1.48E-09	5.30E-09	n.d.	n.d.	8.253 ± 1.699	644.7 ± 9.7	n.d.
1206-R03	1.2810	6.55E-07	3.73E-07	1.33E-01	5.07E+10	6.514 ± 0.030	550.5 ± 4.5	-3.700 ± 0.111
1206-R04	1.1116	1.47E-08	1.36E-07	6.61E-02	2.46E+12	2.982 ± 0.048	618.3 ± 2.7	-1.883 ± 0.116
1206-R05	0.3737	1.07E-08	1.19E-07	1.03E-01	3.51E+12	4.638 ± 0.148	835.9 ± 3.8	-1.288 ± 0.146
1206-R09	1.1223	1.20E-08	1.51E-07	6.55E-02	3.05E+12	2.914 ± 0.055	552.6 ± 2.4	-2.469 ± 0.115

N.B., Unit for abundance is cm^{3}STP/g. n.d.: not detected. Errors for isotopic ratios represent 1 σ uncertainties. Experimental uncertainties in amounts are generally within 10%.